A&A, 714, A262 (2026)
https://doi.org/10.1051/0004-6361/202660845
© The Authors 2026

Astronomy & Astrophysics

Peak 'nebular' emission and early flux excesses in Ca-strong supernovae

C.-G. Touchard-Paxton[1,⋆], K. Maguire[1], C. Frohmaier[2], W.V. Jacobson-Galán[3,⋆⋆], M. Pursiainen[4], C. Angus[5], J. Sollerman[6], A. Polin[7], J. H. Terwel[1], R. Seth[1], C. O'Donnell[1], S. J Smartt[8,5], S. Srivastav[8], A. Bochenek[9], T. de Boer[10], K. K. Das[11], C. Fremling[12,13], A. C. Gordon[14,15], M. J. Graham[13], M. E. Huber[10], C.-C. Lin[10], C. Liu[14,15,16], F. J. Masci[17], P. Minguez[10], G. S. H. Paek[10], J. Purdum[12], B. Rusholme[16], K. Smith[8], R. Smith[12], and R. Wainscoat[10]

[1] School of Physics, Trinity College Dublin, the University of Dublin, College Green, Dublin 2, Ireland
[2] Institute of Cosmology and Gravitation, University of Portsmouth, Portsmouth PO1 3FX, UK
[3] Cahill Center for Astrophysics, California Institute of Technology, MC 249-17, 1216 E California Boulevard, Pasadena, CA 91125, USA
[4] Department of Physics, University of Warwick, Gibbet Hill Road, Coventry CV4 7AL, UK
[5] Astrophysics Research Centre, School of Mathematics and Physics, Queen's University Belfast, Belfast BT7 1NN, UK
[6] The Oskar Klein Centre, Department of Astronomy, Stockholm University, AlbaNova, 10691 Stockholm, Sweden
[7] Department of Physics and Astronomy, Purdue University, 525 Northwestern Avenue, West Lafayette, IN 47907, USA
[8] Department of Physics, University of Oxford, Keble Road, Oxford OX1 3RH, UK
[9] Astrophysics Research Institute, Liverpool John Moores University, 146 Brownlow Hill, Liverpool L3 5RF, UK
[10] Institute for Astronomy, University of Hawai'i, 2680 Woodlawn Drive, Honolulu, HI 96822, USA
[11] Cahill Center for Astrophysics, California Institute of Technology, MC 249-17, 1200 E California Boulevard, Pasadena, CA 91125, USA
[12] Caltech Optical Observatories, California Institute of Technology, Pasadena, CA 91125, USA
[13] Division of Physics, Mathematics and Astronomy, California Institute of Technology, Pasadena, CA 91125, USA
[14] Center for Interdisciplinary Exploration and Research in Astrophysics (CIERA), USA
[15] Department of Physics and Astronomy, Northwestern University, Evanston, IL 60208, USA
[16] NSF-Simons AI Institute for the Sky (SkAI), 172 E. Chestnut St., Chicago, IL 60611, USA
[17] IPAC, California Institute of Technology, 1200 E. California Blvd, Pasadena, CA 91125, USA

Received 8 May 2026 / Accepted 27 August 2026

ABSTRACT

Calcium-strong supernovae (Ca-strong SNe) are a class of thermonuclear transients characterised by rapid photometric evolution (rise times of ≤16 d) and nebular-phase spectra dominated by strong [Ca II] $\lambda\lambda$7291,7324 emission, compared to the strength of [O I] $\lambda\lambda$6300,6364 emission. Despite their unique spectroscopic signatures and association with remote environments at large physical offsets from their host galaxy, their origins remain uncertain. Using new discoveries from surveys such as the Zwicky Transient Facility, supplemented by archival data, we compiled a sample of 46 Ca-strong SNe, including 8 newly classified objects – the largest sample presented to date. We present a comprehensive optical photometric and spectroscopic study of Ca-strong SNe, aimed at better constraining their diversity, progenitor systems, and explosion mechanisms. This includes Gaussian decomposition of the [Ca II] and [O I] nebular emission lines to measure bulk velocities and line profile evolution from peak brightness to deep nebular-phase epochs. Of the 35 Ca-strong SNe with spectra near peak light, we find that 32 objects exhibit significant [Ca II] emission within 10 days of peak. Forbidden [Ca II] emission is typically expected to emerge after the ejecta have expanded, cooled, and reached a sufficiently low density for forbidden transitions to occur. The prevalence of these early features in Ca-strong SNe, however, remains unexplained by current explosion models. In several objects, we identify complex, multi-component line profiles that suggest a transition between two distinct velocity regimes. These transitional features, combined with the common presence of early forbidden emission, lead us to favour a scenario in which extended material surrounds the progenitor and pre-dates the SN itself. Our results suggest that the diverse spectroscopic behaviours of Ca-strong SNe are consistent with white dwarfs exploding in extended environments polluted by prior activity of the progenitor system.

Key words. binaries: general – supernovae: general – white dwarfs

1. Introduction

Ca-strong supernovae are a peculiar and poorly understood class of transients, characterised most prominently by strong forbidden [Ca II] emission in their nebular-phase spectra. For remote Ca-strong supernovae (SNe; objects that occur at extended physical distances from their host galaxy), the prevalence of [Ca II] emission has been interpreted as evidence of sub-Chandrasekhar mass white dwarf (WD) progenitors, as the ejecta of more massive progenitors would continue to burn into heavier elements than Ca, resulting in spectra that would no longer be dominated by [Ca II] emission (Jacobson-Galán et al. 2020;

⋆ Corresponding author: toucharc@tcd.ie
⋆⋆ NASA Hubble Fellow.

Open Access article, published by EDP Sciences, under the terms of the Creative Commons Attribution License (https://creativecommons.org/licenses/by/4.0), which permits unrestricted use, distribution, and reproduction in any medium, provided the original work is properly cited.
This article is published in open access under the Subscribe to Open model. Subscribe to A&A to support open access publication.

Polin et al. 2021). In addition to their strong late-time [Ca II] emission, Ca-strong SNe share a distinct set of photometric and spectroscopic properties: low peak luminosities (−14.0 to −17.5 mag), rapid photometric evolution (rise times ≤16 days), intermediate photospheric velocities (6000–11 000 km s^{-1}), and fast transitions to the nebular phase (Perets et al. 2010; Kasliwal et al. 2012). Their tendency to appear remote from their host galaxies in regions with no underlying star-formation points to old and evolved progenitor systems (Lyman et al. 2014; Lunnan et al. 2017). Despite their faint-and-fast evolving nature and hence low rate of discovery, volumetric rate estimates suggest that Ca-strong SNe may occur at ≥15% the rate of SNe Ia (De et al. 2020), with Frohmaier et al. (2018) predicting they occur as frequently as 33–94%. This makes them an important yet under-sampled population, with implications for both supernova physics and broader astrophysical processes, such as explaining the calcium enrichment observed in the intracluster medium (ICM; Mulchaey et al. 2013).

In our previous study (Touchard-Paxton et al. 2025, hereafter CGTP25), we presented SN 2023xwi – an otherwise typical Ca-strong SN, but notable for displaying strong [Ca II] and [O I] features in spectra taken around peak light. This was highly unusual: forbidden lines such as [Ca II] are not expected to be present until much later phases. Under conventional explosion mechanisms, [Ca II] emission in these objects is expected to occur approximately a few weeks after peak light when the ejecta have become optically thin and the photosphere has receded. This allows the central ejecta to evolve to a low enough density for forbidden emission to occur and, consequently, ensures the SN is well into its nebular phase before this emission can be observed (Dessart & Hillier 2015). The presence of this line at such an early epoch raised the possibility that SN 2023xwi was an indicator of a broader, previously unrecognised behaviour in Ca-strong SNe.

A handful of Ca-strong SNe have been found to display an early photometric flux excess, or pre-peak bumps (PPBs), resulting in double-peaked light curves (e.g. Jacobson-Galán et al. 2022; Ertini et al. 2023). The physical mechanism responsible for these early flux excesses is yet to be fully understood. However, modelling these early phenomena has shown that they can be reproduced by shock cooling emission (SCE) or shock interaction with circumstellar material (De et al. 2018; Jacobson-Galán et al. 2022). The second peak is assumed to be the result of radioactive ^{56}Ni decay. Observations of SN 2019ehk revealed early X-ray emission. The origin of the early flux excess is not necessarily the same as that of the X-rays, but both phenomena indicate significant early-time emission in these objects (Jacobson-Galán et al. 2020; Nakaoka et al. 2021).

Several potential explosion models have been put forward to explain Ca-strong SNe. For example, the Ca-strong object SN 2016hnk was shown to be consistent with both the thick He-shell double-detonation of a sub-Chandrasekhar mass WD (Polin et al. 2019; Jacobson-Galán et al. 2020) and the explosion of a near-Chandrasekhar-mass WD (Galbany et al. 2019). In CGTP25, we proposed a progenitor scenario for the object SN 2023xwi: a recurrent He-nova AM Canum Venaticorum (AM CVn) system in which a WD explodes into an H-poor environment polluted by prior nova eruptions.

In this paper, we investigate the observational behaviour of Ca-strong SNe using the largest sample to date. In Sect. 2, we outline our sample selection, along with their photometric, spectroscopic, and host galaxy properties. In Sect. 3, we present our analysis of the light curves, while in Sect. 4, we present our spectroscopic analysis of the forbidden emission features, including our investigation of transitional features between two distinct velocity components of the [Ca II] emission line. In Sect. 5, we investigate the early flux excess present in many Ca-strong objects, including modelling of the sample using the SCE model. In Sect. 6, we discuss the implications of our results, and in Sect. 7 we discuss how the behaviours of Ca-strong SNe may be compatible with a polluted AM CVn progenitor scenario.

2. Observations

In this section, we detail the sample selection and observations of the Ca-strong objects included in this analysis. In Sect. 2.1, we describe the sample selection of potential Ca-strong SNe from the Zwicky Transient Facility (ZTF). In Sect. 2.2, we detail their photometric and spectroscopic observations, as well as those of one unpublished event from the Panoramic Survey Telescope and Rapid Response System (Pan-STARRS; see Chambers et al. 2016). In Sect. 2.3, we discuss the additional literature Ca-strong SNe considered in our sample.

2.1. Sample selection criteria

ZTF is a wide-field optical time domain survey running on the 48-inch Schmidt telescope (P48) at the Mount Palomar Observatory (Bellm et al. 2019; Graham et al. 2019). The ZTF camera has a 47 square degree field of view and reaches ∼20.5 mag in 30 s, allowing the survey to cover 3750 square degrees per hour at this depth (Masci et al. 2019; Dekany et al. 2020). ZTF's combination of depth and survey speed make it capable of detecting numerous transients, including Ca-strong SNe, at early times across a large fraction of the sky (Graham et al. 2019). As nebular spectroscopy is not achieved for all objects, and this is the primary diagnostic in determining a transient's status as a Ca-strong SN, we implemented similar criteria to De et al. (2020) to extract Ca-strong SNe from the full sample of ZTF objects between 2018 and 2024. Our primary sample within this time period was comprised of any objects spectroscopically classified as a Ca-strong SN using SNID (Blondin & Tonry 2011), and any object that had been classified as SN Ib or Ca-Ia/Ib/Ic on the Fritz science platform[1] (van der Walt et al. 2019; Coughlin et al. 2023), which implements the ZTF alert distribution system (Patterson et al. 2019). Our selection criteria after collating this sample consist of the following:

1. The SN must be fainter at peak than M_r= −17.5 mag after correcting for Galactic reddening, assuming the same redshift as its host galaxy (or nearest viable host, see Sect. 2.4). Host extinction is often negligible in these objects due to their typically remote locations. Ca-strong SNe with small (i.e. ≤3kpc) projected offsets from their host, however, are affected by host reddening. For the eight objects in the full sample of candidate objects for which this was the case, we sourced the host extinction values from their associated publications, where available (see Table B.1). For SN 2024jgw, due to incomplete photometric data, we could not infer the extinction. In instances where the photometric data were not complete enough to constrain the peak luminosity, we compared the decline of the light curve, along with any spectroscopic coverage, to the sample of confirmed Ca-strong objects. If the object did not deviate from the 'expected' behaviour of Ca-strong objects and satisfied the following criteria, we assumed its peak luminosity fell within the

[1] https://fritz2024.caltech.edu/

expected range of $M_r > -17.5$ mag. For objects with no r-band photometric observations, we applied a peak g–r colour correction of 0.51±0.07 mag (see Sect. 3).
2. The spectroscopic properties at peak should be consistent with hydrogen-poor SNe – any objects with distinct broad hydrogen lines were excluded from the sample.
3. The object must evolve into its nebular regime by +30d. This is defined as the combination of a fading continuum and the clear emergence of nebular emission lines, specifically [Ca II] $\lambda\lambda$7291,7324 and [O I] $\lambda\lambda$6300,6364 by this expected nebular-phase threshold. If the only data available are at much later epochs, De et al. (2020) include objects that display a complete transition to the nebular phase by +150 d. For objects with no spectroscopic coverage between +100 and +150 d, we extended the cut-off for satisfying this criterion to the latest epoch within +200 d of peak light.
4. As is standard, we required that any nebular-phase spectrum (after +30 d) that displays both forbidden [O I] $\lambda\lambda$6300,6364 and [Ca II] $\lambda\lambda$7291,7324 emission have a line ratio strength of [Ca II]/[O I] > 2. If multiple spectra were available for an object, the [Ca II]/[O I] ratio was measured at the latest available spectroscopic epoch after +30 d. We determined the lower limit of this ratio for objects with no significant [O I] emission in their nebular-phase spectra by comparing the maximum possible integrated flux in the appropriate [O I] emission region.
5. The object must be spectroscopically distinct at early times from a SN Iax. If it has a strong photospheric-phase spectral match with an Iax on SNID, we excluded it from the sample.

2.2. Newly classified Ca-strong SNe

Applying the selection criteria of Sect. 2.1 to the ZTF 2018–2024 sample, we identify seven unpublished Ca-strong SNe that were ZTF follow-up targets – SN 2021zfp, SN 2023er (Gaia23aet, ATLAS23anl Hodgkin et al. 2023), SN 2023fhk, SN 2024uj (ATLAS24api Tonry et al. 2024), SN 2024jgw, SN 2024uai, and SN 2024aaab. We also include SN 2023ugn, a PanSTARRS object, initially classified as a SN Ib but that fulfils the Ca-strong selection criteria.

Figure 1 shows the photometric evolution of these eight newly identified Ca-strong SNe. Seven of these objects were targetted by ZTF follow-up and were imaged in the ZTF g, r, i bands, with supplementary data from the Asteroid Terrestrial-impact Last Alert System (ATLAS; Tonry et al. (2018); Smith et al. (2020)) in c (4100–6600 Å) and o (5600–8100 Å) bands. The ZTF gri-band data was obtained using the FPBOT package[2]. We removed data with unphysical flux errors, poor PSF fits, images taken through clouds, or those with a failure in the image processing (Rigault et al. 2025). SN 2023ugn was imaged in the PS g, r, i, z bands.

We calculated the Milky Way (MW) extinction for each object using the Schlafly & Finkbeiner (2011) recalibration of the Schlegel et al. (1998) extinction maps and corrected for this assuming a Cardelli et al. (1989) extinction law, with $R_V = 3.1$. Key observational properties of each object (names, redshift, extinction correction, host galaxy name, projected offset from the host galaxy, and nebular [Ca II]/[O I] ratio (see Sect. 2.3), along with the associated references) are given in Table B.1.

The photometric data enables constraints on peak magnitudes, times of peak light, colour evolution, and explosion epochs. Our methodology for determining these is discussed in Sect. 3. Of these eight objects, only four objects were observed throughout the SN's rise, peak, and decline: SN 2023er, SN 2024gjw, SN 2024uai, and SN 2024aaab. A further three have data allowing us to estimate the peak time through a comparison with other Ca-strong objects: SN 2021zfp, SN 2023ugn, and SN 2024uj. The remaining object, SN 2023fhk was only observed during its decline so its time of peak light and peak r-band magnitude could not be constrained.

Spectra of the eight newly identified Ca-strong SNe were sourced from a variety of telescopes. Each SN has between one and eight spectra at phases of −7 to +125 d, relative to inferred r-band peak (see Sect. 3) – these are presented in Fig. B.1. The telescopes and instruments of the spectra are listed in Table B.2, along with the phases relative to the time of r-band peak. We corrected each spectrum for redshift and MW extinction, and have masked strong host galaxy emission features from the spectra of SN 2022psx and SN 2023fhk.

In each object with a spectrum after peak light (all except SN 2023er), there is a clear [Ca II] $\lambda\lambda$7291,7324 emission feature in the photospheric (< +14 d) spectra (often offset from rest wavelength by up to 6000 km s^{-1}; see Fig. 5), often accompanied by the emergence of [O I] within a few days. The spectroscopic evolution of the six SNe with multiple epochs is broadly consistent with previous observations of Ca-strong SNe, exhibiting relatively fast transitions from the photospheric to the nebular phase. While the signal-to-noise (S/N) and wavelength coverage vary between SNe, the core features, particularly the [Ca II] line, remain prominent in all events at later times. Unlike the other objects presented, SN 2023fhk grows redder as the SN evolves. This peculiar behaviour cannot be further investigated photometrically due to the lack of g-band observations at phases similar to those of the observed spectroscopy.

2.3. The full Ca-strong sample

In addition to these 8 new events, we collated published Ca-strong SNe and Ca-strong candidates, resulting in a total sample of 66 candidate Ca-strong SNe, at z of ∼0.004–0.04. Their key properties, along with their associated references are given in Table B.1. These 66 events include 8 that were reclassified as Ca-strong SNe from other types (see Appendix A for further details). To ensure consistency, we applied the same cuts of Sect. 2.1 to the full sample. Following criterion four of the selection criteria, we cut all candidates with [Ca II]/[O I] < 2 after +30 d from peak light where data was available. For objects with no spectral observations after +30 d (marked by † in the [Ca II]/[O I] column of Table B.1), we compared their available data with other Ca-strong SNe at similar phases. Both the photometric and spectroscopic properties of each object without nebular-phase spectral observations was consistent with the behaviours observed across the Ca-strong sample; we therefore continued to classify each as Ca-strong.

Applying these cuts removed 20 candidates. Two objects, SN 2019gsc and SN 2019ttf, were removed due to their prior classification of, and strong spectroscopic match with, SNe Iax. Of the 12 objects excluded due to a low [Ca II]/[O I] ratio, three (SN 2018jak, SN 2012hn, and SN 2021pb) were previously classified as Ca-strong (Valenti et al. 2014; Das et al. 2023). However, as their measured [Ca II]/[O I] ratios fall below our adopted threshold (SN 2012hn: 1.63±0.01 at 149 d; SN 2018jak: 1.01±0.03 at 109 d; SN 2021pb: 1.27±0.01 at 109 d), we excluded them. SN 2018jak and SN 2021pb additionally exhibit broad H lines in their photospheric-phase spectra, which independently disqualifies them based on our selection criteria. The remaining

[2] https://github.com/simeonreusch/fpbot

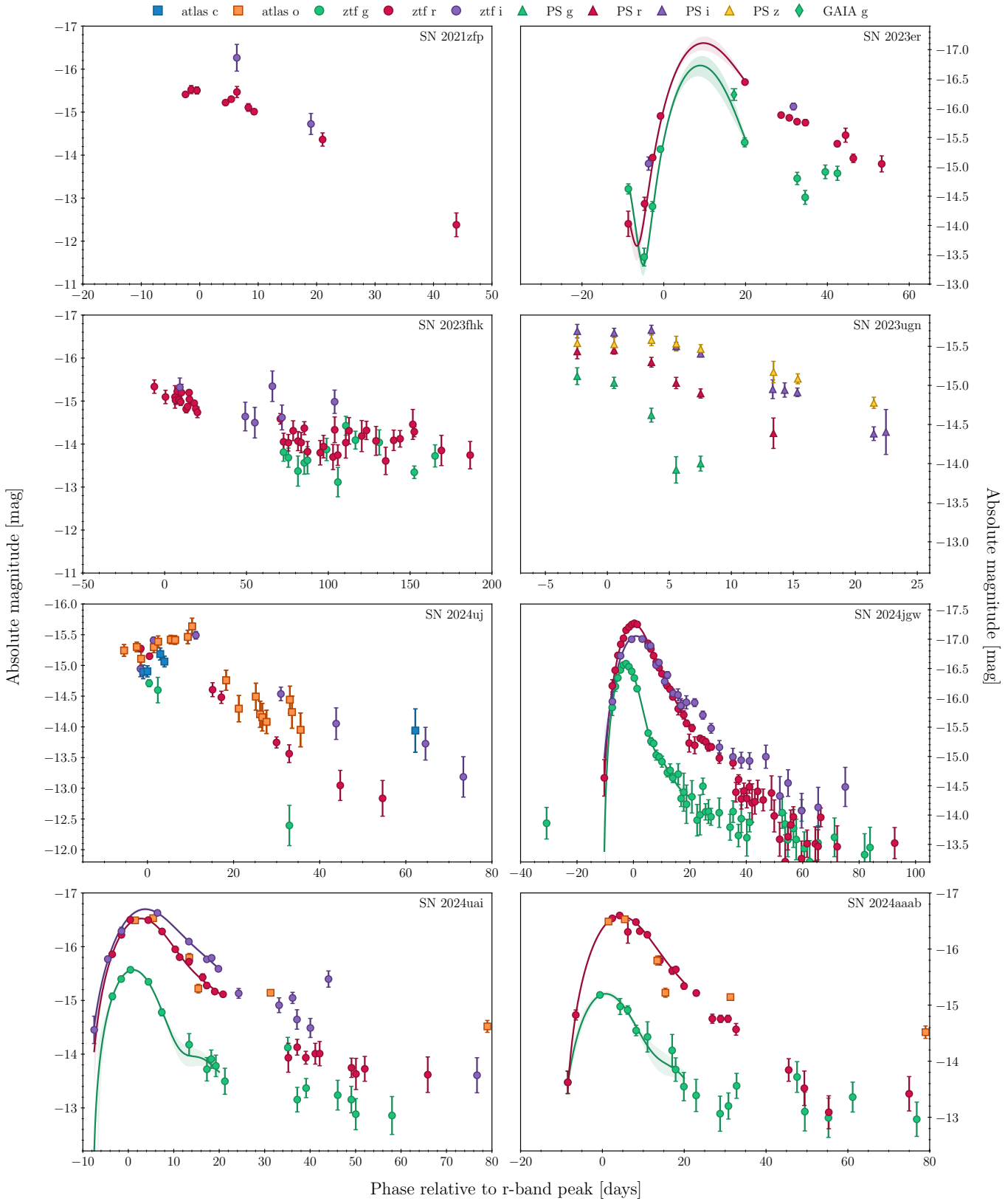


Fig. 1. Optical light curves for each of the eight confirmed new Ca-strong SNe in our sample. The optical data points are plotted with the following markers: ATLAS *c*-band (blue squares), ATLAS *o*-band (orange squares), ZTF *g*-band (green circles), ZTF *r*-band (red circles), ZTF *i*-band (purple circles), PANSTARRS (PS) g-band (green triangles), PS *r*-band (red triangles), PS *i*-band (purple triangles), PS *z*-band (yellow triangles). The solid lines represent the light curve fits as a result of our Gaussian processing fitting procedure (see Sect. 3).

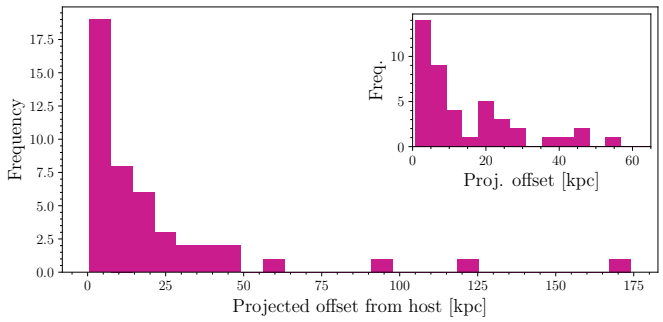


Fig. 2. Histogram of the physical separation of each Ca-strong object in our sample from its host. Inset: Histogram of objects with separations of <60 kpc, removing three objects (iPTF11kmb, SN 2019bkc, and SN 2023er).

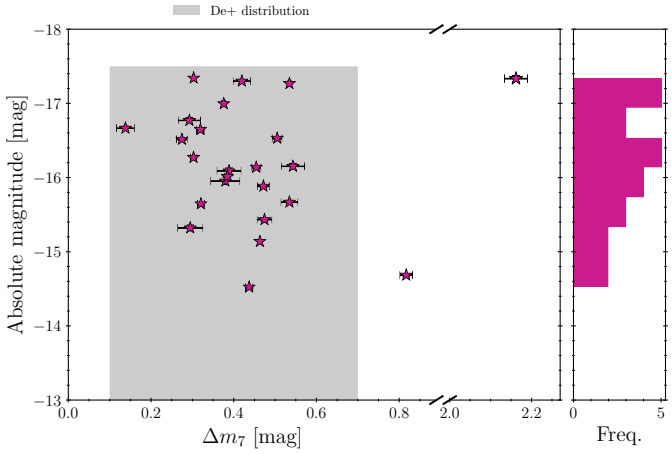


Fig. 3. Absolute peak r-band magnitude against $\Delta m_7(r)$. The parameter space for Ca-strong SNe from De et al. (2020) is shaded in grey.

six objects were disqualified for displaying broad H lines in their photospheric spectra. Our final sample consists of 46 confirmed Ca-strong SNe.

2.4. Host galaxy properties

For objects with no previously assigned host galaxy, we determined the host to be the nearest galaxy with a measured redshift that was consistent with the forbidden [Ca II] NIR triplet emission line in the latest spectral epoch for that given object. All objects in the sample of Ca-strong objects have a viable candidate host with a measured spectroscopic redshift. We therefore assumed the redshift of each object to be that of its host galaxy and calculated the luminosity distances using these redshift values, correcting for host-galaxy peculiar velocities where available. We determined the projected physical offset of each object from its host by measuring the angular separation between the transient position and the host galaxy centroid and converting this to a projected physical distance (Table B.1).

As discussed in Sect. 1, Ca-strong transients display a preference for early-type galaxies, as well as group and cluster environments, suggestive of old stellar populations (Lyman et al. 2014; Lunnan et al. 2017). Figure 2 shows a histogram of the separation of confirmed Ca-strong objects in our sample from their hosts. The weighted mean of the distribution 5.76 ± 0.75 kpc, and a median of 9.90 kpc. Lunnan et al. (2017) report a median projected offset of 8–30 kpc (dependent on the exact sample definition) for a previous smaller literature sample, while Srivastav et al. (2026) using a sample of Ca-strong transients discovered by ATLAS (and which are a subset of our sample) report a median projected offset of ∼11 kpc. Our median value is slightly lower than these but not significantly different. As shown by previous samples such as Lunnan et al. (2017), the projected offset distribution of Ca-strong transients is more offset than the normal SN Ia distribution and ∼25% of the objects in our sample still occur at offsets of >20 kpc (and two at >100 kpc). These trends imply, therefore, that these objects can still be considered 'remote' objects compared to typical SNe Ia.

3. Peak light photometric properties

For objects with well-sampled light curves around peak, we fitted them using a Gaussian process (GP) regression (see Fig. 1). Gaussian process regression is a non-parametric Bayesian approach that models the light curve as a distribution over functions, rather than assuming a fixed template (Williams & Rasmussen 2006). This makes it particularly well-suited for our sample of SNe, wherein cadence and noise properties vary between objects (e.g. Dimitriadis et al. 2025). We adopted a squared exponential kernel with an added white-noise term to describe the smooth evolution of the light curves in combination with associated photometric uncertainties and varied-cadence data for each object in our sample (Roberts et al. 2013). We optimised the length scale and amplitude of the kernel for each object using `emcee` to determine the parameters with the maximum likelihood.

From the GP fits, we determined the time of peak brightness in order of preference: r, g, i, and finally the ATLAS c and o bands. Since the time of peak can differ between filters, prioritising r-band ensured consistency across the sample given its most consistent coverage. Uncertainties on the time of peak r-band brightness, $t_{\rm peak}$, were estimated from the GP predictive variance, marginalised over the kernel parameters. Additionally, the GP fits provided measurements of the absolute magnitude at peak, $g-r$ colour at peak, and the r-band decline rate, $\Delta m_7(r)$, defined as the change in magnitude in the first 7 days post-maximum light (Table B.3).

Of the full sample of 46 confirmed Ca-strong SNe, 34 objects had sufficient optical light curve data for determining $t_{\rm peak}$, including four of the new SNe shown in Fig. 1. For the eight literature objects with no observations in the appropriate range (SN 2000ds, SN 2001co, SN 2003H, SN 2003dg, SN 2005E, iPTF15eqv, SN 2018lqu, and SN 2018gwo), we adopted times of the r-band maximum from their discovery papers. For the new objects with no photometry around peak light (SN 2021zfp, SN 2023fhk, SN 2023ugn, and SN 2024uj), we estimated their time of peak by cross-matching their photometry with more well-constrained Ca-strong objects in our sample. As SN 2023fhk was discovered post-peak, the first detection of this object at MJD 60036 marks the upper limit of its time of peak light. Where r-band data were not available, we determined photometric behaviour from g-band data, applying a correction of $t_{\rm peak_r} = t_{\rm peak_g} + 2$ d, based on the mean $\delta t_{\rm r,peak\text{-}g,peak}$ of 2.0±0.2 d across the sample of objects with sufficient coverage in both bands around peak light.

Figure 3 shows the distribution of absolute peak r-band magnitudes and $\Delta m_7(r)$ – the decline in r-band magnitude in 7 days following peak light – for the 24 objects of the full Ca-strong sample with r-band observations around peak light. Consistent with the previous study of De et al. (2020), which is shown in

grey in Fig. 3, the population is confined to faint peak luminosities ($M_r \gtrsim -17.5$ mag) and rapid post-peak declines ($\Delta m_7 \geq 0.1$ mag). All objects bar two in our sample – SN 2021inl and SN 2019bkc (which has been independently noted for its extraordinarily rapid evolution; see Prentice et al. 2020), which evolve faster than the rest of the sample – fall within this expected parameter space, reinforcing the classification of Ca-strong SNe as faint, fast-evolving explosions. We note, however, that the definition of this class is partially circular, since the faintness (peak r-band magnitude fainter than −17.5 mag) and rapid evolution are themselves used in the classification. To ensure that this faintness requirement did not introduce bias by excluding more luminous, yet otherwise 'typical', Ca-strong SNe, we examined all objects in our original sample satisfying the remaining classification criteria but failing the brightness cut. No such objects were identified.

We determined the g–r colour at peak of the 24 Ca-strong objects with peak photometry in both g− and r-bands. All are red at peak, and the distribution is peaked at a g–r colour of 0.51±0.07 mag, with colours ranging from 0.42±0.01 to 1.64±0.01 mag. This exceptionally red object, which is an outlier from the rest of our sample, is SN 2021sjt. This SN is located in a spiral arm, suggesting this may be at least partially explained by host-galaxy extinction.

4. Spectroscopic analysis of forbidden emission features

CGTP25 find that forbidden transition emission lines, specifically [Ca II] $\lambda\lambda$7291,7324, [O I] $\lambda\lambda$6300,6364, and [O I] λ5577, can be observed from as early as peak light. This observation, which is in contradiction with traditional understanding (i.e. that these nebular emission lines should only be visible when the ejecta have expanded and cooled) is a potential indicator of a more complex progenitor system than previously thought. Callan et al. (2025) find the merger of a 0.6 $M_\odot$ CO WD and 0.4 $M_\odot$ He WD can reproduce spectroscopic evolution consistent with Ca-strong SNe. In their model, [Ca II] emission begins to become prevalent at +20 d – earlier than the typical threshold of +30 d by which Ca-strong SNe are expected to evolve to their nebular regime (De et al. 2020). This emission, however, remains substantially delayed from the observed peak light [Ca II] emission of SN 2023xwi presented in CGTP25. To quantify the extent of this phenomenon – i.e. whether the early emission of these forbidden features was unique to this object or if it is common across the sample of Ca-strong SNe – we investigated its presence and behaviour throughout the sample of Ca-strong objects.

4.1. Single Gaussian fitting to forbidden emission lines

The non-local thermodynamic equilibrium (NLTE) model of a He-shell detonation of a CO WD presented by Dessart & Hillier (2015) produces faint and fast light curves, similar to those of Ca-strong SNe. Their synthesised spectra produce strong Ti II features in the spectral region, which we identify as [Ca II] emission, and blended Sc II and Ti II contributions in the [O I] emission region. These models are significantly reddened due to line-blanketing as a result of the large Ti II abundance – a phenomenon we do not observe in Ca-strong SNe. Similarly, the model presented by Callan et al. (2025) is significantly reddened due to the predicted high abundance of Ti II. We do not observe this high degree of reddening across the sample of Ca-strong

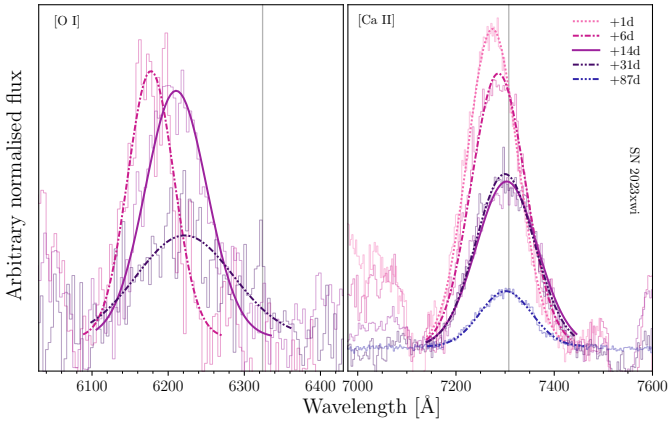


Fig. 4. Example local pseudo-continuum-corrected emission line model fit of the [O I] (left) and [Ca II] (right) feature in SN 2023xwi throughout its evolution. The spectra are overlaid with their total model profile fit. The vertical grey line shows the weighted average of the two component wavelengths of each forbidden emission feature at rest.

SNe at peak light, and therefore assume the features in these regions to be [Ca II] and [O I], respectively.

To model the emission features of each of the forbidden emission lines of [Ca II] $\lambda\lambda$7291,7324, [O I] $\lambda\lambda$6300,6364, we modelled each feature as a combination of the local pseudo-continuum and the profile of the emission lines. The local pseudo-continuum was approximated by a linear relation between wavelength and observed flux between the two local minima of the feature. The emission profile of both the [Ca II] and [O I] features were modelled with a singular Gaussian profile as the two component emission lines of these doublets could not be confidently resolved in any spectra. Due to convolution with the instrument resolution of each spectrum (Maguire et al. 2012), a single Gaussian model is the simplest plausible empirical analogue to the observed emission profiles. We fitted all spectra for every object in our sample using this methodology. Example model fits to the [Ca II] and [O I] regions for SN 2023xwi are shown in Fig. 4.

Uncertainties were calculated using a Monte Carlo approach, in which the start and end points of the fitting region were varied based on the resolution of any given spectrum. For higher-resolution spectra (resolution <2 Å), the fitting boundaries were perturbed by nine times the spectral resolution. Medium-resolution spectra (2–10 Å) were varied by six times the resolution, while low-resolution spectra (resolution >10 Å) were permitted a maximum fixed variation of 55 Å. Each model was refitted 1000 times per spectrum, with random sampling of the start and end points. The mean and standard deviation of the resulting velocities were taken as the measured velocity and its associated uncertainty, respectively. Fits in which the uncertainty was both greater than 300 km s^{-1} and exceeded 20% of the mean value of the measured velocity offset were further investigated to ensure the measured velocity was associated with the correct spectral feature. This uncertainty was then combined with the uncertainty associated with the measured redshift, as well as the uncertainty associated with the resolution of the spectrum itself, resulting in the total velocity uncertainty at each spectral epoch.

In cases where both the [O I] $\lambda\lambda$6300,6364 and λ5577 features were present, the velocity of the [O I] λ5577 line was used as a check to verify the identification of the [O I] $\lambda\lambda$6300,6364 feature – the velocity offset associated with each of these two [O I] emission lines has been shown to be in agreement within

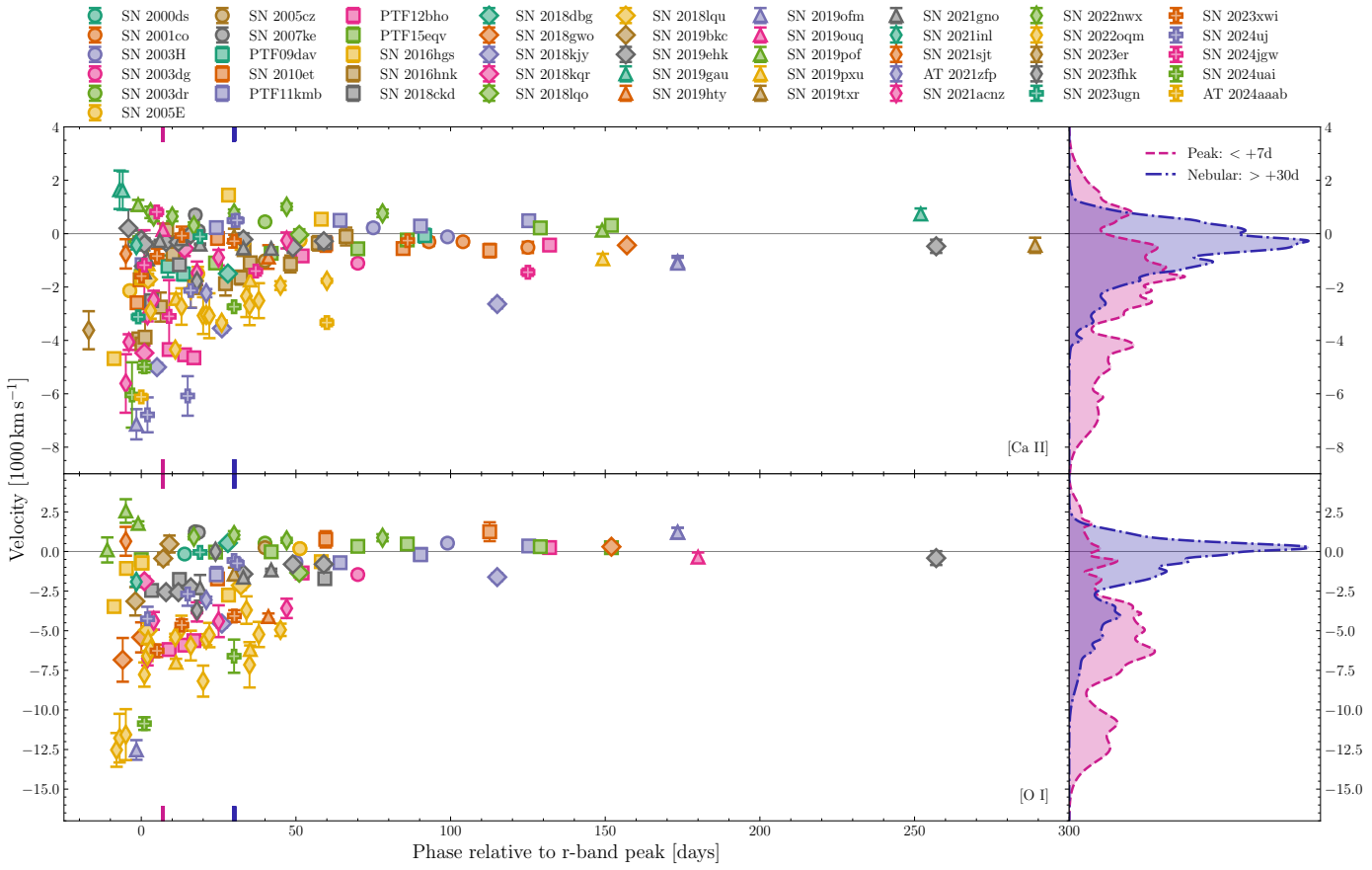


Fig. 5. Left panels: measured forbidden emission line velocities of [Ca II] $\lambda\lambda$7291,7324 (upper) and [O I] $\lambda\lambda$6300,6364 (lower). Right panels: distribution of velocities for the forbidden transition emission [Ca II] (upper) and [O I] (lower). The peak (spectrum closest to peak per SN at < +7 d, dashed pink) and nebular (the latest spectrum taken per SN at > +30 d, dot-dashed blue) distributions – constructed by summing the Gaussian probability distributions of each velocity – overlaid and normalised with respect to the nebular distributions. The cut-off point for the peak distribution (+7 d) and the start of the nebular distribution (+30 d) are shown by pink and blue tick marks, respectively, on the left subplots.

3σ throughout an object's full spectral evolution (see Sect. 5.2 of CGTP25). If the measured [O I] $\lambda\lambda$6300,6364 and λ5577 velocities agreed within a 3σ significance level, the identification of the feature as [O I] was deemed reliable. For objects with no clearly distinguishable [O I] λ5577 emission, if the measured velocity of the presumed [O I] $\lambda\lambda$6300,6364 feature was within the range of expected values (−14 000 to +2500 km s^{-1}, derived from spectra with confirmed [O I] emission) we assumed the feature had been correctly identified as [O I].

To ensure the same feature was measured at all epochs for a given SN, the pseudo-equivalent widths of each feature were measured at each epoch. A feature was confirmed to be the same spectral emission line for pseudo-equivalent widths that were consistent across all photospheric epochs within a 5σ threshold across all observations before +14 d of peak light. In the photospheric phase, the continua of Ca-strong SNe is complex and therefore, the 5σ limit was chosen to account for any discrepancies in the pseudo-continuum approximation. For all analysed lines in our sample, no such features were re-classified.

In our full sample of 46 Ca-strong objects, all displayed prominent [Ca II] emission. Forty-two objects had distinct [O I] $\lambda\lambda$6300,6364, 35 of which were verified by their [O I] λ5577 feature. Of the 35 objects in our full sample which were spectroscopically observed within 7 d of peak light, 29 had measurable forbidden [Ca II] emission in their peak spectra. If this is extended to within 10 d of maximum, 32 of the 35 objects with spectra around this epoch display distinct [Ca II] emission. In all objects with later observations, this feature persisted in the spectra through the nebular phase, remaining visible in the latest spectrum of each object.

The velocity evolution of the [Ca II] and [O I] $\lambda\lambda$6300,6364 features (relative to their mean rest-frame wavelengths) for each SN are shown in the upper and lower panels of Fig. 5, respectively. The velocities of both forbidden emission features generally evolve from a broad range of non-zero velocities in the photospheric spectra – defined as those before +30 d from peak – to a velocity consistent with zero velocity at late times. The dashed pink histograms in the right panels of Fig. 5 show the distribution of velocities from spectra taken closest to peak brightness for each object, all within +7 d of peak.

We measured the weighted mean velocities of the distribution of peak spectra with respect to their associated uncertainties to be −2290±830 km s^{-1} for [Ca II] and −6040±1400 km s^{-1} for [O I] $\lambda\lambda$6300,6364. The distribution of [Ca II] velocity has a broad spread of σ = ±2260 km s^{-1}, and extreme redshifted and blueshifted velocities spanning 1600±700 km s^{-1} (SN 2019gau at −7 d) and −6800 ±700 km s^{-1} (SN 2024uj, +2 d), respectively. Similarly, the peak velocity distribution of [O I] is broad with σ = ±4110 km s^{-1}, and extremes of 2600±700 km s^{-1} (SN 2019pof, −5 d) and −12 500±1000 km s^{-1} (SN 2022oqm, −8 d; Irani et al. 2024). Any objects with a redshifted velocity around peak light (as opposed to a blueshifted velocity as seen across the rest of the sample) have emission line offsets consistent with 0 km s^{-1} to, at most, a level of 3σ.

In contrast, the nebular-phase spectral velocities, shown as dot-dashed blue histograms in Fig. 5, corresponding to the latest available spectra for each SN (taken after +30 d from peak) exhibit notably narrower distributions than at maximum light. The mean velocities of these late-time spectra are -690 ± 350 km s^{-1} for [Ca II] and -1550 ± 810 km s^{-1} for [O I] $\lambda\lambda$6300,6364, which are consistent with zero velocity within 2σ.

The transition from a broad and offset distribution at peak, to a narrower, near-zero distribution at late times may be the result of emission originating from different regions of Ca-strong SNe as they evolve. The forbidden emission we observe in the nebular-phase spectra is likely a result of core-dominated emission as expected at these epochs. Conversely, the presence of these forbidden transition emission lines around peak light with distinctly non-zero velocities implies a separate origin for the early-time emission. This early-phase emission may arise from material that is pre-existing and external to the SN explosion itself, as observed in SN 2023wxi (CGTP25). The physical interpretation is discussed further in Sect. 6.2.

In addition to the evolution of each forbidden line, throughout the full spectral evolution of each object in the sample of Ca-strong SNe, only five spectra show [O I] emission associated with a 'slower' intrinsic velocity than [Ca II] at the same epoch with a significance level of $>3\sigma$. In all other cases, the [O I] emission is blueshifted to a greater velocity than the [Ca II].

4.2. Two-component [Ca II] fitting

CGTP25 hypothesise the presence of 'transition features' in the spectra of Ca-strong SNe. These are the spectral signatures of the transitional phase between the early-time offset velocity feature and core-dominated emission feature of the SN. Of the sample of 46 Ca-strong SNe, we have spectra at a high enough resolution in the correct phase range ($\sim$ +14– +30 d from peak) for 26 objects to study these transition features. At earlier phases, the traditionally 'nebular' emission is obscured by the photosphere, and we did not model this spectral feature at early times with the two-component model. Due to contaminating emission lines at the wavelength of the [O I] feature, as well as its weaker strength into the nebular phase compared to [Ca II], our investigation into transition features is focussed solely on the [Ca II] feature.

To determine if transitional features were present, the [Ca II] emission profile in spectra after +14d was modelled as a model comprised of two Gaussian profiles (one for the higher-velocity offset emission and one for the lower-velocity emission) after we continuum-corrected each spectrum. Uncertainties were calculated using the same Monte Carlo-based approach as outlined in Sect. 4.1. The inclusion of an additional Gaussian component introduces two degrees of freedom to the model and thus often produces a lower residual than the single-Gaussian model. We therefore evaluated each model using criteria, which penalise this increased model complexity: the Akaike information criterion (AIC; Akaike 1974) and Bayesian information criterion (BIC; Stone 1979). They are defined as

$$\mathrm{AIC} = -2\ln(\mathrm{L}) + 2k \quad (1)$$

and

$$\mathrm{BIC} = -2\ln(\mathrm{L}) + k\ln(\mathrm{N}), \quad (2)$$

with likelihood, L, number of model parameters, k, and number of data points, N. For each best-fit, we calculated the AIC and BIC values using `RegscorePy` – a Python package that aids model comparison with the use of various regression models. The Akaike information criterion does not penalise as harshly as BIC, and therefore the favoured model using AIC may be overfitting the data. Conversely, BIC penalises harshly for additional parameters, and will favour the simplest appropriate model. This can result in a favoured model that is an over-simplification of the underlying physical mechanisms. Due to these intricacies, it is best to optimise a fit with respect to both the AIC and BIC values.

Negative values of ΔAIC and ΔBIC (where ΔAIC(BIC) is the difference between the AIC(BIC) values for the double- and single-component Gaussian models per epoch) indicate a preference for the double-component model, with values of $\Delta\mathrm{AIC} \leq -5$ and $\Delta\mathrm{BIC} \leq -2$ indicating a strong preference for the two-component model of [Ca II] emission during the transitional phase (Kass & Raftery 1995; Burnham & Anderson 2004). These values indicate that the fit improvement exceeds that expected solely from the additional free parameters in the double-component model. In Table B.4, we present ΔAIC and ΔBIC between double- and single-component Gaussian models for each spectrum in the transitionary period, as well as later time spectra to determine if these features persist.

All Ca-strong objects with spectra within the expected phase range of transitional features (+14 to +30 d) prefer the double-Gaussian fit, indicative of two distinct emission components, potentially arising from two distinct emitting regions. Example single- and double-component fits to the [Ca II] feature are shown for SN 2018kjy in the left panels and for SN 2023wxi in the right panels of Fig. 6. This preference for a double-peaked emission profile is not due to the doublet nature of the [Ca II] emission feature as the velocity separation of our measured two components is significantly larger than the separation of the [Ca II] doublet component lines in all cases.

While the double-component Gaussian model is preferred throughout the sample of Ca-strong SNe, we note this does not necessarily require two distinct emitting regions. Alternative ejecta structures and geometries can produce emission line profiles that are similarly approximated by a double-component Gaussian model. A shell-like distribution of Ca, for example, could produce a flat-topped [Ca II] profile, while a disc or ring-like structure could produce a 'double-horned' emission line (Jerkstrand 2017). As we observe the emergence of a persistent 'high-velocity' component at a significantly earlier epoch than the 'low-velocity' component, we favour a system in which the two Gaussian components are representative of two distinct emitting regions. In such a system, the low-velocity component arises from a secondary emitting region as the SN transitions into the nebular regime. While we observe this trend in Ca-rich SNe with multiple spectral observations from peak light, through the transitional phase, and into the truly nebular regime, we cannot definitively conclude that this behaviour is consistent throughout the sample of Ca-strong SNe. The observed velocity evolution associated with the forbidden [Ca II] and [O I] emission lines is consistent with our interpretation of two distinct emitting regions, and we therefore favour this interpretation. We note, however, that as multi-epoch spectra spanning the relevant evolutionary phases were not observed for each object, we cannot definitively rule out the possibility that Ca-strong SNe constitute a heterogeneous class in which similar observed profiles and evolution arise from different underlying ejecta geometries.

A handful of transition features were still observable well into the traditionally purely 'nebular' regime, with the transition features of six objects (SN 2003H, iPTF15eqv, SN 2018gwo,

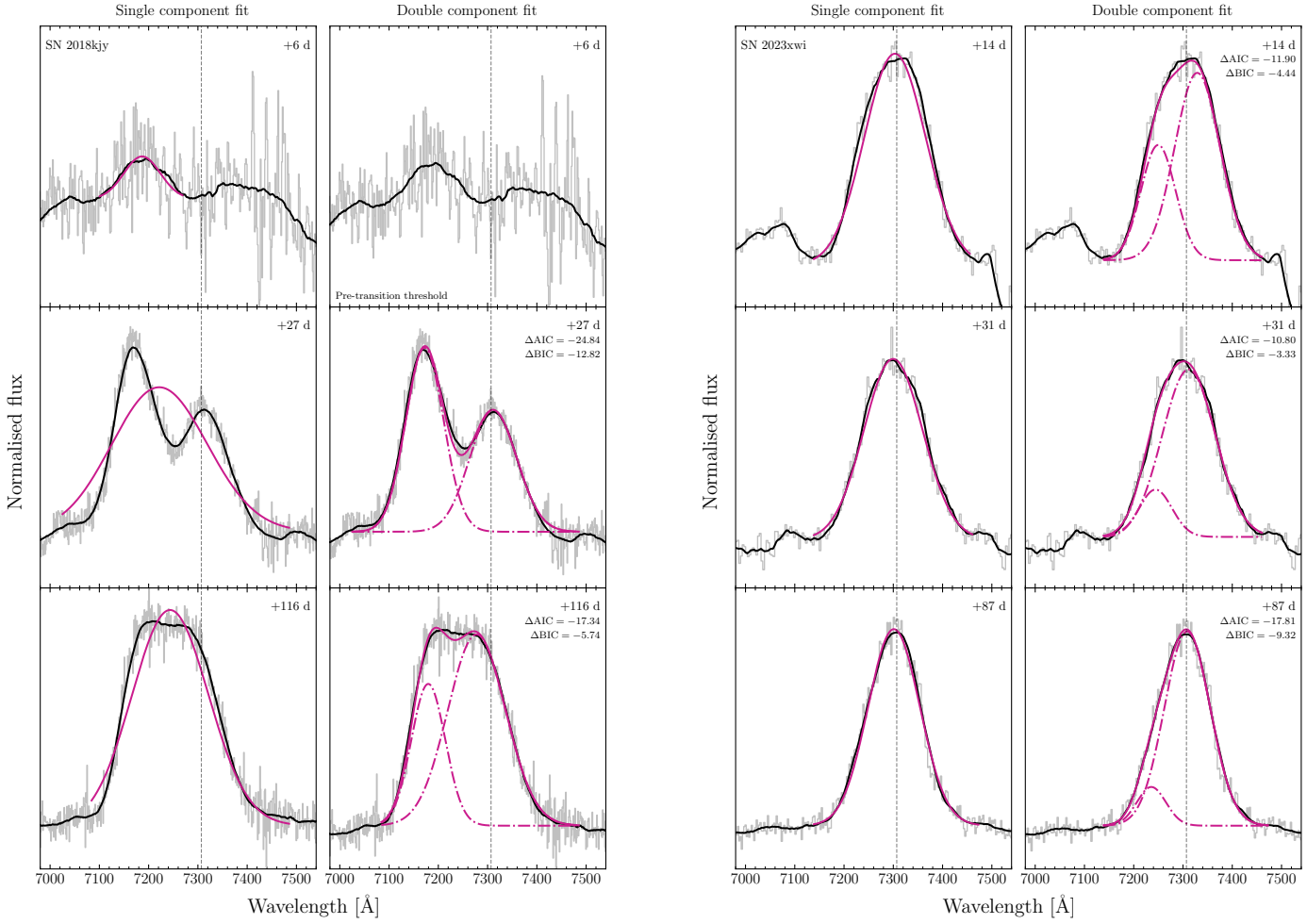


Fig. 6. Example [Ca II] single- and double-component Gaussian mixture model fits for SN 2018kjy (left) and SN 2023xwi (right). The pseudo-continuum-corrected spectrum (light grey) is overlaid with a Savitzky-Golay smoothed spectrum for display purposes (black). The total model profile fit is shown with a solid pink line. The dot-dashed pink lines show the component Gaussians. The left panel for each object shows the single Gaussian fit across the full spectral time series, and the right panel shows the double Gaussian profile for each of the spectra observed after the transition threshold. The vertical dashed line corresponds to the weighted mean rest wavelength of the [Ca II] feature.

SN 2018kjy, SN 2019ofm, and SN 2019pof) remaining observable until well after +100 d. This could suggest that these have a stronger contribution from a region external to the SN, allowing it to be seen until late times. This is discussed further in Sect. 7.2. This persistent contribution from the 'high-velocity' component deep into the nebular regime may contribute significantly to the overall integrated line flux of the [Ca II] emission feature at these late epochs. As these are the spectra from which we determine the [Ca II]/[O I] ratio of each object – a key diagnostic tool in their classification – it is therefore plausible that these ratios are overestimates of the 'true' ratio of emission fluxes produced by the core of the SN. The contribution from the 'high-velocity' component at these late epochs is, however, minimal as the 'low-velocity' component tends to dominate the line profile. In the latest available spectrum of SN 2018kjy, which has the most prominent 'high-velocity' component persisting into the nebular regime, the 'high-velocity' component contributes ≤25% flux to the overall emission profile. Additionally, as the [Ca II]/[O I] ratios of these objects with persistent 'high-velocity' components are comfortably above the threshold value of 2, we are confident each of these objects are true members of the Ca-strong class and have not been misclassified.

Of the 26 objects with spectra after the expected transitionary threshold, only four spectral epochs do not have values of ΔAIC and ΔBIC that indicate a preference for a two-component fit to the [Ca II] emission feature: SN 2019ofm at +173.4 d, SN 2010et at +84.6 d, SN 2005cz at +40.0 d, and SN 2022oqm at +60 d. As we selected the most appropriate model with respect to both of these criteria and each of these spectra lie outside our expected phase range for transitional features, we disregard these four spectral epochs in our analysis of the transitional feature.

Figure 7 shows the velocity and full width at half maximum (FWHM) evolution with time of each of the component velocities in each object. The 'high-velocity' and 'low-velocity' labels are relative for a given SN – the high-velocity feature is defined as the component of the emission feature with the greatest blue-shifted velocity, and the low-velocity feature is that with the least blue-shifted velocity. The velocities of both the high-velocity and low-velocity components of the [Ca II] emission features remain constant within 3σ. For objects iPTF15eqv and SN 2022oqm, their redshifted 'low-velocity' components are investigated in Fig. 8. The [O I] emission in both objects is consistent with a velocity of 0 km s^{-1}. Both the Ca II NIR $\lambda\lambda$8498,8542,8662 and [Ca II] features, however,

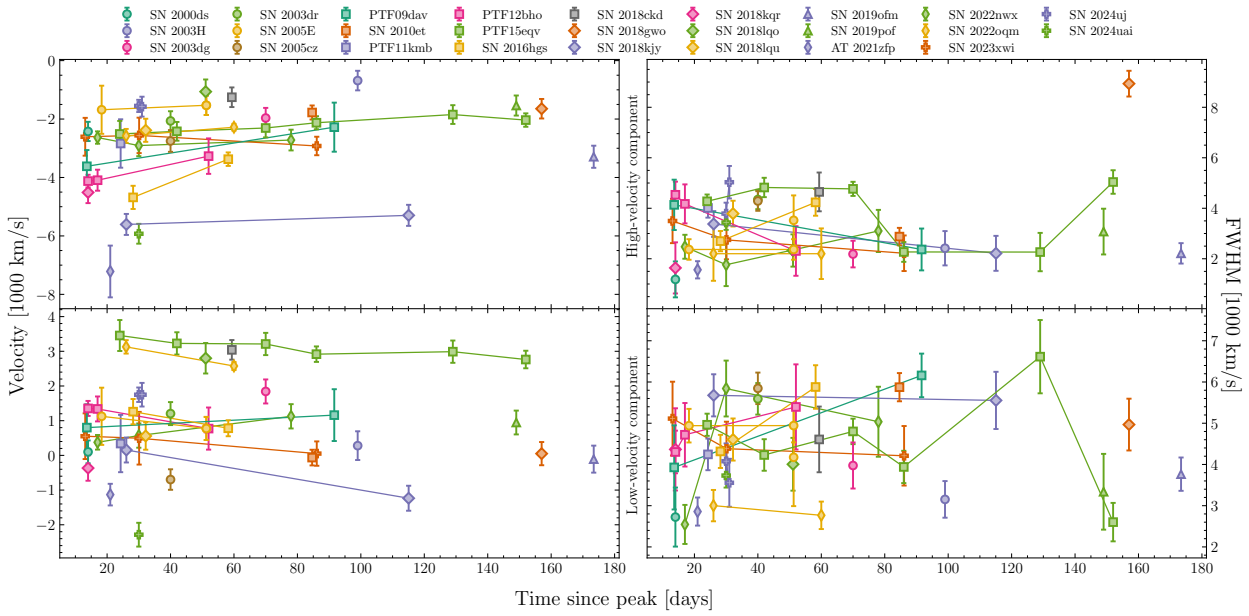


Fig. 7. Velocity and FWHM evolution of the double-component Gaussian model for the [Ca II] feature. Left sub-panel: velocity evolution of the high-velocity component (upper) and low-velocity component (lower). Right sub-panel: FWHM evolution of the high-velocity component (upper) and low-velocity component (lower).

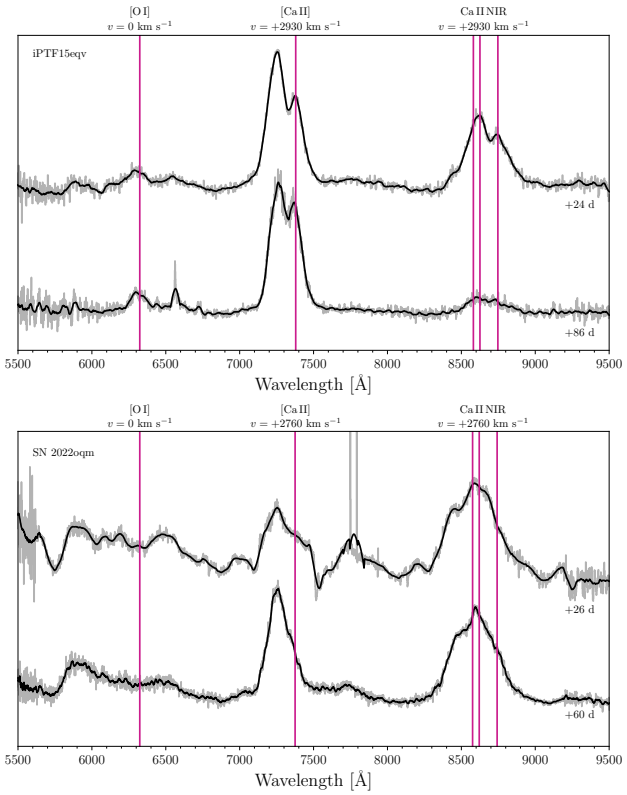


Fig. 8. Two spectral epochs of objects iPTF15eqv (upper) and SN 2022oqm (lower). The vertical pink lines show the rest wavelength of the [O I] emission feature and the [Ca II] and Ca II NIR features at the velocity associated with the 'low velocity' component. For both objects, their significantly redshifted 'low-velocity component' [Ca II] emission aligns with the velocity of the Ca II NIR feature.

are instead consistent with the mean measured velocity of the 'low-velocity' component of their respective objects (Fig. 7), indicating the redshift we observe is not unique to the [Ca II] emission feature, but an offset in both nebular Ca emission features.

The FWHM of the high- and low- velocity components remain constant as each object evolves to within 3σ, with the exception of SN 2022nwx. Determining the true FWHM at each epoch requires us to accurately identify the start and end wavelength of each component of the [Ca II] emission line, which is difficult due to the complex nature of the photospheric phase spectral continuum. Additionally, this analysis assumes the only contributing flux to each emission component is from [Ca II] emission. Any contribution to these line profiles as a result of blended features with other species will artificially broaden the feature. Although, as discussed, we do not expect significant contamination from other features. As a result, the uncertainties of the FWHM measurements are significantly higher at earlier epochs. Additionally, the anomalous behaviour of SN 2022nwx may be attributed to a misidentification of the start and end points of its low-velocity component in the earlier epochs. Despite this source of increased uncertainty, the evolution – or lack thereof – of the FWHM of each component provides valuable insight into the behaviour of Ca-strong SNe. A constant FWHM through time points towards emission from a region, which is fixed in velocity-space. We can therefore infer each of the emitting regions, from which our distinct emission components may arise, are fixed in velocity-space.

5. Photometric analysis of early-flux excess

Previous investigations into the early photometric behaviour of Ca-strong objects have shown they can display an early flux excess (or PPB) (Jacobson-Galán et al. 2020, 2022), with distinct deviation in their early-time light curves from the rise of the main, ^{56}Ni-powered, peak. In our full sample of 46 Ca-strong objects, 26 objects were photometrically observed between −16 and −5 d from peak light, and as such are included in this section of the analysis. A preliminary classification of the early flux excess was determined by visually inspecting the light curves

for our sample for deviations from a smooth rise between −16 and −5 d. Objects with at least two photometric observations in one band that deviated distinctly from an otherwise smooth rise were labelled as 'present bump' objects. Those with no clear deviation were labelled as 'no bump' objects, and objects that were either not sampled at a high enough cadence pre-peak to determine this or had ambiguous bump presence were labelled as 'possible bump' objects. No object in our sample has pre-peak data of sufficiently high cadence to definitively rule out the presence of a bump. Of these 26, 15 objects were categorised into the 'present bump' category: SN 2018kjy, SN 2018lqo, SN 2018lqu, SN 2019ehk, SN 2019hty, SN 2019ouq, SN 2019pof, SN 2019txr, SN 2021acnz, SN 2021gno, SN 2021inl, SN 2021sjt, SN 2022nwx, SN 2022oqm, and SN 2023er. The remaining 11 objects were classed as 'possible bump' objects based on this initial visual inspection: SN 2018ckd, SN 2018dbg, SN 2018kqr, SN 2019gau, SN 2019ofm, SN 2019ouq, AT 2021zfp, SN 2023er, SN 2024jgw, SN 2024uai, and AT 2024aaab. These preliminary categories guided the initial analysis technique applied to each object: 'present bump' objects were modelled using the methodology outlined in Sect. 5.3, and 'possible bump' objects with that described in Sect. 5.4.

5.1. Early flux excess in other SNe

Early flux excesses have been observed in various types of SNe. In Fig. B.2, we display the *r*-band light curves of each of our 'present-bump' objects, compared to the light curves of three other distinct SNe with known pre-peak emission – SN 2017cbv (SN Ia, Hosseinzadeh et al. 2017), iPTF15dtg (SN Ic, Taddia et al. 2016), and SN 2011fh (SN IIb, Pessi et al. 2022). Each subplot displays one of our objects in direct comparison to these comparison objects, scaled to the peak brightness of each Ca-strong object. In this section of analysis, we do not assume that the physical origin of the early flux excesses are the same between Ca-strong SNe and these other classes exhibiting an early flux excess. We rather use these comparisons to constrain the differences in occurrence time and duration of the flux excesses.

Across our Ca-strong sample with these early bumps, there is clear deviation in the behaviour of their photometric data and those of the comparison objects. The first deviation is present in the decline rate and shape of the main peak of the light curves: the Ca-strong sample decay much faster after peak than any of the three comparison objects, resulting in narrower light curves. Notably, SN 2019ehk, SN 2019pof, and SN 2021sjt – which were previously classified as SNe IIb-Ca-strong (Das et al. 2023) – show significantly faster light curve evolution than the type IIb comparison event, serving as further evidence that they are likely 'true' members of the Ca-strong class, as discussed in Sect. 2.1. Additionally, the comparison SN Ia and SN Ic objects have much less prominent PPBs than the Ca-strong objects that exhibit this phenomenon. The PPB of SN 2017cbv, for example, manifests more as a broadening of the light curve at early times rather than a distinct rise-and-decline behaviour as seen in many Ca-strong objects (e.g. SN 2019ehk, SN 2019ouq, and SN 2021sjt).

Another clear distinction between the light curves of these comparison objects and the Ca-strong events are in the behaviour of the PPB itself. The timescale of the PPBs in Ca-strong SNe appear to occur over shorter timescales than in the other classes of SNe. While the exact duration of each PPB in the Ca-strong sample cannot be constrained, in well-sampled objects such as SN 2019ehk, we see that Ca-strong early flux excesses typically have a timescale of ∼5 d from start to finish. The comparison SNe, however, have much longer timescales of this early flux excess: the decline of SN 2011fh (as its full early flux excess behaviour was not observed) lasts ≤6 d, the PPB of SN 2017cbv extends over ∼10 d, and the PPB timescale of iPTF15dtg is constrained to t ≥ 10 d – each implying larger timescales than any observed PPB across our Ca-strong sample.

5.2. Shock cooling emission model

Piro (2015) describe a generalised prescription of SCE and provide a time-dependent light curve model to describe the first peak of double-peaked light curves, which we apply to our sample. It was previously used to model the high-cadence double-peaked early time light curve of SN 2019ehk (Jacobson-Galán et al. 2020). This SCE model approximates the luminosity produced when an explosion shock deposits energy into a low-mass extended envelope of mass M_e, and radius R_e, surrounding a core of mass M_c. The SCE model is a one-zone model. It assumes a constant density in the homologously expanding and spherically symmetric extended material and is agnostic to its specific chemical composition and thus is especially well suited to the unknown progenitor composition of Ca-strong SNe. These assumptions limit the extent to which the derived envelope masses and radii can be disentangled; thus, the derived values in this section of analysis can only serve as estimates on the 'true' values of the envelopes surrounding each Ca-strong object.

Following the analytic treatment of Valenti et al. (2008), as discussed by Jacobson-Galán et al. (2020), the ejecta mass, M_{ej}, and kinetic energy, E_k, of a SN are related by

$$M_{ej} = \frac{10}{3}\frac{E_k}{v^2}, \tag{3}$$

where v is the photospheric velocity of the ejecta. Ca-strong SNe typically have been found to have M_{ej} of 0.1–1.5 $M_\odot$, and v of 5000–11 000 km s^{-1} (De et al. 2020). Using these ranges in Eq. (3) yields an expected E_k range of 1.5×10^{49}–1.1×10^{51} erg.

5.3. SNe with pre-peak bumps

Our implementation of the SCE model computes the bolometric luminosity of the model, converts it to band-specific fluxes, and performs MCMC fitting to our photometric data using the `emcee` ensemble sampler to infer the physical parameters (M_e, R_e; Foreman-Mackey et al. 2013). We used a fixed core mass of 0.6 $M_\odot$. As a test of our model implementation, we fit the light curves of SN 2019ehk using the same opacity (κ = 0.2 cm^2 g^{-1}) and SN energy ($E_{SN} = 1.8\times10^{50}$ erg) as in Jacobson-Galán et al. (2020). We find best-fit parameters of $M_e = 0.006 \pm 0.001\ M_\odot$ and $R_e = 146 \pm 22\ R_\odot$, consistent with the values of Jacobson-Galán et al. (2020) to 1.3σ, despite a change in the core mass from 1 to 0.6 $M_\odot$.

To investigate early flux excesses in our Ca-strong SN sample, we applied this analytic SCE model to the observed photometry of each event. All photometric measurements from ZTF and literature sources were binned nightly prior to fitting. For photometry of literature objects, which were only available in magnitudes, we converted these to comparable flux units. We defined a 'non-detection' as any measured flux with a significance of less than 3σ. To ensure that only the early flux excess was modelled with this SCE approach, we restricted the fit to data between the latest non-detection prior to first light and the onset of the main light curve rise for each SN (typically −16 to −5 d pre-peak) – this value was chosen manually per SN.

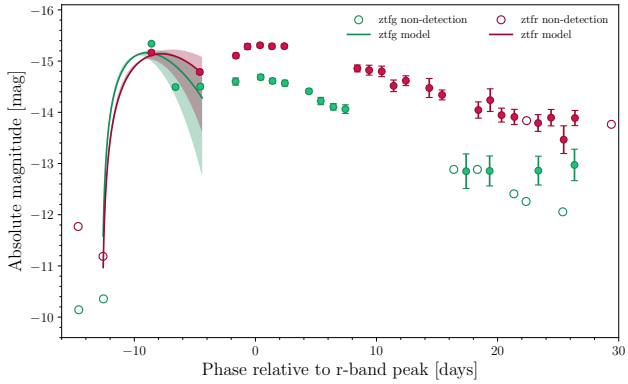


Fig. 9. Early flux excess SCE fit to SN 2022nwx. The solid points show ZTF data at a significance level of >3σ, and open points show non-detections for ZTF $g-$ (green) and $r-$ (red). The $g-$ and r-band models are fitted simultaneously, and are shown with the solid red and green lines, respectively, with their associated 1σ uncertainties shaded.

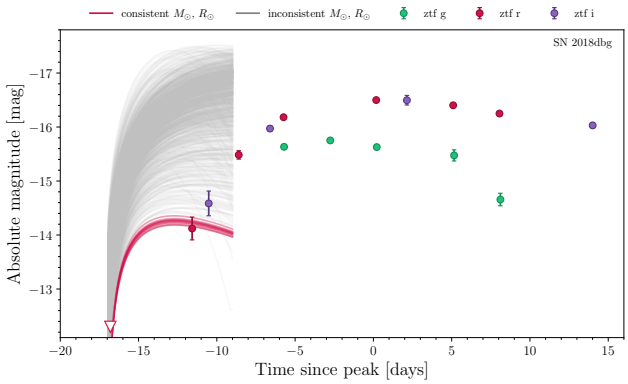


Fig. 10. SCE model fitting procedure to determine the upper limits of M_e and R_e for a 'possible bump' object – SN 2018dbg. The green, red, and purple points show the ZTF g-, r-, and i- band photometric observations. The grey lines represent SCE models of M_e and R_e parameter combinations, which are inconsistent with the observed r-band photometric data. The red lines represent SCE models, which are consistent with the r-band observations.

Using a grid search combined with MCMC sampling, we fitted the model simultaneously to the multi-band light curves of each event at 15 fixed explosion energies between 1.5×10^{49}–1.1×10^{51} erg as derived above, determining the best-fit energy from the associated model with a reduced chi-squared value closest to 1. Given the well-constrained nature of the SN 2019ehk early light curve fits, we used its fitted SCE parameters as our prior centroids in the fitting for the rest of the 'present bump' sample. We used logarithmic priors with ranges of M_e = 0.01–0.51 $M_\odot$ and R_e = 10–5000 $R_\odot$. Upper limits of these priors were chosen based on the largest model values of Piro (2015), while the lower limits were chosen as 0.02 times the smallest model values of Piro (2015) to account for the comparatively lower luminosities of Ca-strong SNe.

The posteriors from our MCMC sampling provided marginalised constraints on M_e and R_e. We took the median values and 16th and 84th percentile intervals as the estimated parameter value and its associated 1σ uncertainties, respectively. We generated synthetic light curves using the best–fitting parameters, and compared them directly to the binned multi–band photometry. Figure 9 shows an example of the best fitting light curve for SN 2022nwx in our 'present bump' sample.

5.4. SNe with possible pre-peak bumps

The SCE models for each of the 15 events in our sample with confirmed bumps were used to evaluate whether an early flux excess could be ruled out in our 'possible-bump' sample of 11 objects. For each object, the range of permitted pre-peak fluxes from our SCE model outputs was compared to the observed light curve. We adopted a criterion that an early bump would be considered undetected if the predicted flux does not exceed 3σ above the local photometric uncertainty. Objects with upper limits below the predicted flux of all models were considered as not showing a bump, whereas objects with non-constraining limits were flagged as potential SCE candidates. No objects in our sample were originally visually classified as 'no bump' objects, nor did they satisfy the criterion required to be categorised as 'no bump' objects here, and as such all remaining Ca-strong SNe in our sample were deemed to be 'possible bump' objects.

For the objects flagged as 'possible bump' candidates, we determined the upper limits of M_e and R_e that were consistent with each object's observed photometry. Figure 10 shows the SCE model fitting procedure we used to determine the upper limits of M_e and R_e for a 'possible bump' object – SN 2018dbg. Taking the SCE model with the highest flux consistent with the photometry – the red line with the brightest absolute magnitude in Fig. 10 – gives the model with the highest M_e and R_e consistent with observations. These values of M_e and R_e therefore serve as the upper limit estimates for this object. If any objects had data of a high enough cadence to constrain an SCE model fit further than just an upper limit – i.e. more than two photometric data points describing the rise and decline of the PPB in any given band – we re-classified these into the 'present bump' sample. This was the case for objects SN 2019hty and SN 2019txr, which were added to the 'present bump' sample, and the full range of permitted pre-peak fluxes from our SCE model outputs (as described above) was re-determined. As these objects had values of M_e and R_e consistent with the rest of the 'present bump' sample, their inclusion into this sub-sample did not alter our previously determined range of expected values of M_e and R_e in Ca-strong objects.

If the time between the last non-detection and first 3σ detection was less than 10 days, we classed the model as consistent with the photometry if the model and observed data were in agreement within 1σ. For those with no photometry within this range, we could neither rule-out the presence of a PPB nor constrain any physical parameters of the explosion environment. We randomly sampled a grid of physically plausible M_e and R_e values, derived from the fits of the sample with clear early flux excesses, and derived the associated Piro (2015) models associated with each combination of values for a fixed E_{SN}. E_{SN} was fixed at the lowest value preferred across the objects with a confirmed bump – $3.31\pm0.03\times10^{50}$ erg s^{-1}. Using this value of lowest plausible SN energy ensured the M_e and R_e values derived from this analysis were true upper limits on the ejecta required to reproduce the observed behaviour.

5.5. SCE fitting results

While the SCE modelling can confidently reproduce this early photometric phenomenon observed in many Ca-strong objects in our full sample, there is still clear diversity between each of these objects. Figure 11 shows the M_e against R_e parameter space of these model fits of our sample of Ca-strong events. The dashed lines denote the range of values expected for typical SNe IIb –

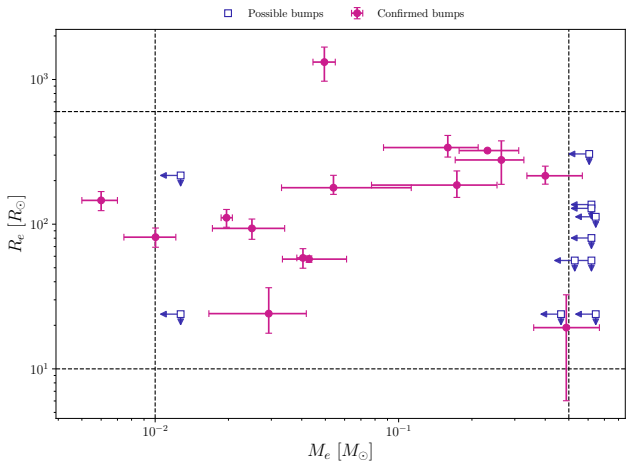


Fig. 11. Parameter space of envelope mass and radius for all 'present bump' and 'possible bump' objects across our sample. The solid pink circles show the derived M_e and R_e for 'present bump' objects. The open blue squares represent the upper limits of M_e and R_e associated with each of the 'possible bump' objects. The dashed lines denote the range of values expected for typical SNe IIb.

the most prominent subclass of object with early flux excesses (Nakar & Piro 2014; Arcavi et al. 2017). Each of the 'confirmed bump' parameters lie within 3σ of the range of values for SNe IIb. The PPBs in our sample (see Fig. B.2) show a broad range of behaviours, with peak brightnesses of between -14.32 ± 0.04 (SN 2021gno) and -17.33 ± 0.02 mag (SN 2022oqm), durations of ~5 d (SN 2019ehk) to ~9 d (SN 2022oqm).

A key caveat to the methodology we employed is that it assumes the extended material is symmetric and spherical. Any asymmetries in the progenitor system would vary both the mass and radius along the line of sight and could significantly impact the luminosity of a 'bump' due to SCE of this external material.

Among the sample of objects with higher-cadence photometric observations across this typical phase range of Ca-strong early flux excesses (i.e. >2 distinct epochs between last non-detection and first 3σ detection), each object fell into the 'present bump' category. Without high-cadence data within this critical range of -16 and -5 d in which we would expect a PPB to occur, it is impossible to fully constrain the behaviour of any early flux excess in the 'possible bump' sub-category, or to rule out the presence of a bump entirely. As Ca-strong objects are intrinsically faint, they often are not detected until past this critical range of phases. Despite these observational challenges, over half of the objects from our total Ca-strong sample are observationally consistent with an early flux excess. 33% of objects in our sample fall into the 'present bump' sub-class, with a further 24% defined as 'possible bump' objects; the remaining objects are unfortunately excluded from this area of analysis due to insufficient data (see Sect. 5). As such a significant proportion of these objects show this behaviour, and we cannot definitively rule out the presence of a bump in any Ca-strong object in our sample. However, we may speculate that these PPBs may be a phenomenon common across this class of transient.

6. Discussion

6.1. Widespread detection of early forbidden features

One of our primary objectives was to identify and characterise, in a large sample of Ca-strong SNe, any early [Ca II] and [O I] emission, such as that observed in the Ca-strong object SN 2023xwi (CGTP25). From our full sample of 46 Ca-strong SNe, 35 objects had the required spectra within 7 d of peak, and of these 35, 29 had measurable forbidden [Ca II] emission in this phase range. If we extend this 'peak' cut-off to 10 d, this increases to 32 of the 35 total objects (91%) having early forbidden [Ca II] emission. The physical environment responsible for forbidden emission features, traditionally only seen at late times due to the low-density requirements for its associated atomic transition, must therefore be common in Ca-strong SNe.

Forbidden emission typically emerges once the ejecta have expanded, cooled, and become optically thin, and the photosphere itself has receded. This observed early time forbidden emission is therefore difficult to reconcile with an intrinsic origin, as the ejecta are expected to be too dense at these phases for strong forbidden emission to occur.

The NLTE CO+He WD model of Ca-strong events presented by Callan et al. (2025) produces distinct [Ca II] emission by +20 d–10 d earlier than the typical expected threshold phase for the emergence of nebular emission lines in Ca-strong objects. This is, however, still at a considerably later phase than we observe across the sample of these events, with 91% of objects displaying distinct [Ca II] emission within +10 d of peak light. While these results demonstrate that forbidden emission can occur earlier than traditionally expected, the observed early-time spectroscopic behaviour of Ca-strong SNe is still yet to be reproduced by models for Ca-strong SNe.

Peculiar ejecta structures, such as steep density gradients, may permit the emergence of forbidden emission lines at earlier epochs than typically expected (e.g. Bose et al. 2025). While we, therefore, cannot rule out an intrinsic ejecta origin for the early [Ca II] emission observed in Ca-strong SNe, such behaviour has yet to be reproduced around peak light across the full population of these objects. We instead favour an interpretation in which the observed early-time [Ca II] emission originates from an external, low-density region of Ca that predates the SN explosion, naturally providing the conditions required for early forbidden emission.

The same is true for the observed [O I] emission, indicating that this external region of matter must, at least, include a combination of low density Ca and O. When originating from the same emitting region, [Ca II] emission typically dominates any [O I] emission as cooling via [Ca II] emission is far more efficient than through [O I] – the Einstein A coefficient of [Ca II] is two orders of magnitude greater than that of [O I] (Jacobson-Galán et al. 2022). To observe both forbidden emission lines concurrently, we therefore require either substantially higher abundances of O than Ca, or the emitting regions to not be co-located. The range of non-zero velocities around peak light of the [Ca II] and [O I] emission in the sample of Ca-strong SNe places further constraints on the external, pre-existing, environment of these objects and is likely the result of different viewing angles, thus implying that the potential progenitor systems are inherently aspherical.

6.2. Forbidden velocity evolution and transition features

As discussed in Sect. 6.1, the early forbidden [Ca II] and [O I] emission lines likely originate from an external low-density region but as the ejecta expand and cool and the photosphere recedes, we expect the [Ca II] and [O I] features to instead be dominated by the core SN emission at late times. This would present itself as an evolution in velocity space from a non-zero velocity around peak to a zero velocity at late-times. This

evolution of velocity is seen in our SN sample (see Fig. 5), indicating that for Ca-strong SNe, the source of forbidden emission may transition from a low density external region in the photospheric phase, to a more core-dominated emission regime in the nebular phase.

Figure 7 shows the velocity and FWHM evolution of each component velocity for each of the SNe with observed transition signatures in the [Ca II] emission profile. Both the high- and the low-velocity components of the [Ca II] emission line for each SN remain constant with time. We suggest that these high-velocity and low-velocity components are the physical counterparts to the external-structure-dominated emission region (high-velocity component) and the core-dominated emission region (low-velocity component). This indicates that the line profile evolution we see in each of these objects, such as that seen of SN 2023xwi in Fig. 4, is not a result of the deceleration of any external, pre-existing material as the SN enters the nebular regime. Instead, the profiles we observe may be indicative of the relative increase in core emission, which ultimately dominates over the external emission in the nebular regime, resulting in our final observed velocities of these forbidden lines that are broadly consistent with zero velocity. As shown in Fig. 8, for the objects with an offset 'low-velocity' emission component, this apparent redshifted velocity is consistent with the velocity of the NIR triplet emission. Therefore, while their 'low velocity' component is not necessarily consistent with 0 km s^{-1}, it is still consistent with the nebular Ca emission associated with the SN.

Currently, rapid classification of candidate Ca-strong events for follow-up relies on criteria such as a low absolute magnitude and a H-free spectrum. Incorporating searches for early-time [Ca II], and in most cases [O I], which is typically detected within 7 d from first [Ca II] detection, could significantly improve early classification. This would enable more targeted follow-up, ensuring fewer observational resources are spent on candidates that ultimately prove not to be Ca-strong.

6.3. Early flux excesses in all Ca-strong SNe?

In our full sample of 46 Ca-strong objects, 15 had distinct early flux excesses in their light curves. When we include the further 11 objects with at least one photometric point that deviated from a smooth rising light curve, all 26 Ca-strong objects with pre-peak observations are consistent with an early flux excess. Additionally, there is no SN in our sample for which we can definitively rule out the presence of an early flux excess. The 'present bump' and 'possible bump' objects span the full range of observed peak brightnesses and redshifts of the full Ca-strong sample, suggesting the presence of a PPB is not magnitude limited, and detection is instead dependent on early-time sampling of the light curves. The high fraction of Ca-strong objects in which we see a PPB, despite the observational challenges, indicates that they may be a common trait across all Ca-strong SNe.

We find timescales for the PPB of 5–9 d and peak brightnesses of ~ -14.3 to -17.3 mag. In Fig. 11 we presented the parameter space of envelope mass and envelope radius for all 26 objects in our sample of Ca-strong SNe for which we could constrain the SCE model or estimate upper limits on the parameters that would produce an SCE model consistent with our observations. We find envelope masses of 0.006–0.54 $M_\odot$ and envelope radii of 24–1320 $R_\odot$ for those that could be modelled.

To explore potential physical connections, we investigated correlations between early flux excesses and spectroscopic features, including the velocities of early forbidden lines, as well as other photometric properties. Comparisons between the 'present bump' and 'possible bump' populations were made to assess whether they represent distinct subgroups within the Ca-strong class. Figure 12 shows the [Ca II] (upper) and [O I] $\lambda\lambda$6300,6364 (lower) velocities against the derived envelope mass and radius values. There is no obvious correlation between the early forbidden emission line velocity, and either the envelope mass or radius. Due to the intrinsic degeneracy between M_e and R_e in and thus the limitations of, the Piro (2015) model, it is not unexpected that no such correlations were found. Future modelling of Ca-strong SNe and their progenitor environments, which are not dependent on the same assumptions of spherical symmetry and a constant density profile may reveal a correlation between these parameters.

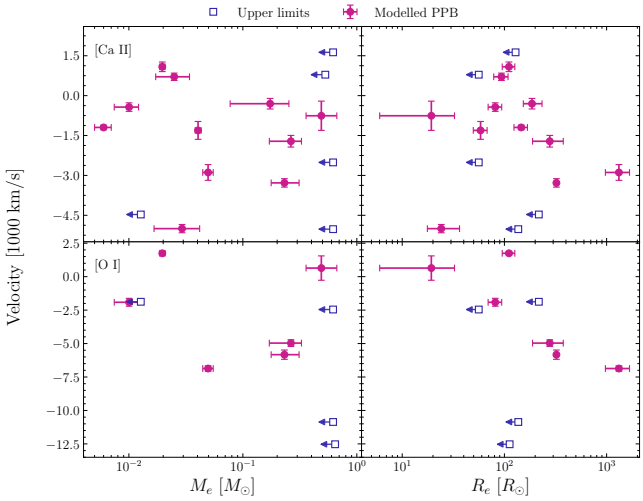


Fig. 12. Velocity at peak of forbidden [Ca II] (upper) and [O I] (lower) and envelope mass (left) and radius (right) required to reproduce the observed photometric early flux excess behaviour. The pink circles show the values associated with the 'present bump' sample, and the open blue squares show the upper limits associated with the 'possible bump' objects.

6.4. Ca-strong sub-classifications

De et al. (2020) introduce further sub-classification of Ca-strong objects: Ca-strong-Ia and Ca-strong-Ib/Ic. This is based on the line depth of the Si II λ6150 feature, $a_{\mathrm{Si\,II}\,\lambda6150}$ at peak light, as defined by Sun & Gal-Yam (2017). They report that 'normal' SNe Ia and SNe Ib/Ic are split (see figure 9 of Sun & Gal-Yam 2017), with $a_{\mathrm{Si\,II}\,\lambda6150} > 0.35$ for SNe Ia and $a_{\mathrm{Si\,II}\,\lambda6150} \leq 0.35$ for SNe Ib/c. Using the same method, we measured this for all Ca-strong objects in our sample with spectra around peak light with a resolution of $\leq$20 Å and S/N $\leq$3 to ensure correct identification and accurate modelling of the feature. From our full sample of 46 confirmed Ca-strong objects, 18 objects do not meet these criteria. The resulting values for the remaining 28 objects are shown in Table B.7. In addition to the sub-classification of De et al. (2020), we introduce a Ca-strong-ambiguous class – objects for which their measured $a_{\mathrm{Si\,II}\,\lambda6150}$ and associated uncertainties are consistent with the Ia/Ibc boundary of $a_{\mathrm{Si\,II}\,\lambda6150} = 0.35$ within 3σ.

Of the 29 SNe with spectra around peak light (within +7 d from r-band maximum), only one object – SN 2016hnk – is definitively Ca-strong-Ia. Five further objects fall in the Ca-strong-ambiguous class (iPTF09dav, SN 2018lqo, SN 2018lqu, SN 2019ofm, and SN 2021inl), and the remaining 23 objects

fall into the Ca-strong-Ib/Ic classification. As SN 2016hnk does not exhibit properties that significantly differ from those of other Ca-strong SNe (i.e. values of M_{peak}, $\Delta m_7(r)$, $v_{[Ca\ II],\ peak}$, $v_{[O\ I],\ peak}$ are all comparable to that of the rest of the sample), there is no strong justification for subdividing these events into Ca-strong-Ia and Ca-strong-Ib/Ic sub-classes. Additionally, such sub-categorisation can imply that 'Ca-strong-Ia' and 'Ca-strong-Ib/Ic' have different physical origins. The continuous range of spectroscopic and photometric behaviours we observe across our full sample of Ca-strong SNe, however, along with the remote origins of many being incompatible with core-collapse origins (Lyman et al. 2014; Dong et al. 2022), makes such a distinction misleading. We therefore disregard this avenue of sub-categorisation of Ca-strong SNe, and instead assume these objects are not comprised of distinct heterogenous subclasses.

7. Implications for the progenitors of Ca-strong SNe

As discussed in previous sections, the early presence of [Ca II] and [O I] emission lines, along with the velocity evolution of these features, point towards Ca-strong progenitors occurring in environments with low-density, external regions comprised of (at least) Ca and O. Early forbidden emission lines have also been observed in the super-luminous SN, SN 2019szu (Aamer et al. 2024). This object exhibits pre-maximum [O II] emission, attributed to an O-rich CSM produced by mass-loss episodes shortly prior to explosion. The prominent forbidden emission we observe across the sample of Ca-strong SNe is therefore indicative of Ca-strong SNe occurring in similarly polluted environments.

Modelling Ca-strong SNe and their potential progenitors demonstrates that their mid-to-late time behaviour (i.e. after 14d) can be reproduced by interacting He+C/O WD systems (Zenati et al. 2023; Morán-Fraile et al. 2024; Callan et al. 2025). The presence of forbidden emission around peak light, however, is still yet to be reproduced without prior pollution of the surrounding environment. CGTP25 proposed a progenitor environment polluted by a recurrent He-nova AM CVn system, based on observations of the Ca-strong object SN 2023xwi. Our analysis shows that the behaviours observed in SN 2023xwi were not unique to that specific object but are instead common across the Ca-strong class. Therefore, we investigated whether this proposed origin of SN 2023xwi can be extended to describe the origins of all Ca-strong SNe.

In this proposed progenitor system, we hypothesise that Ca-strong SNe arise from recurrent He-novae AM CVn-type systems, resembling V445 Puppis (Kato & Hachisu 2003; Woudt et al. 2009). In such systems, a CO WD accretes He from a H-deficient companion and undergoes recurrent He-novae (Roelofs et al. 2007). He is swept up from the He-shell of the WD(s) and forms polar outflows along the axis of rotation of the binary system. From the surface of the CO WD(s), O also gets swept up into these lobes, creating low-density O regions within the broader lobe structure. In more violent novae, small abundances of elements up to Ca can be synthesised. These, too, get swept up into the lobes and form low-density Ca regions within this structure. These aspherical and asymmetrically distributed low-density elements, ejected prior to the SN explosion, can explain the presence and kinematic evolution of [Ca II] and [O I] features in both the photospheric and nebular phases once the SN finally explodes. For a detailed schematic and explanation of this system, please see Sect. 6.1 of CGTP25.

7.1. Peak forbidden line emission from polar outflows from a recurrent He-nova AM CVn system

When the SN explodes – before the ejecta overtake the regions of O and Ca within the lobes, and while the photosphere is still obscuring the core of the SN – we observe forbidden [Ca II] and [O I] emission from this external lobe structure. The velocities we observe of these forbidden emission line features at early times give insight into the velocities of the low-density Ca and O in the lobes. Figure 6 of CGTP25 shows a 2D schematic of our proposed progenitor system – adapted from the V445 Puppis system (Woudt et al. 2009) – and highlights the viewing-angle dependence on the observed velocity. In such a system, the minimum velocities observed around peak correspond to observations orthogonal to the rotation axis of the WD system, and the maximum peak velocities occur when such a system is observed down the axis of the lobes. The expected observed velocity distribution in such a system should follow a broadly Gaussian distribution, with the peak falling at a non-zero velocity. Viewing the system directly down the lobe, resulting in the maximum observed velocity, will be the least likely viewing angle.

The maximum velocity we observe at peak, therefore, could correspond to the intrinsic velocity of the outflow lobes, assuming the progenitor systems of these objects are all broadly uniform. The velocity distribution of [O I] emission – the forbidden emission line with the highest observed velocity per object throughout our sample – around peak light has a mean value of -6040 ± 1400 km s^{-1}. The greatest observed velocity associated with a forbidden emission line in the sample of Ca-strong objects is $-12\,500 \pm 1000$ km s^{-1} (SN 2022oqm, −8 d; Irani et al. 2024). While this is greater than the observed polar outflow of V445 Puppis, the only such system for which this has been measured, it is plausible that other AM CVn-type systems with greater polar outflow velocities. In addition, due to the range of peak brightnesses reached by Ca-strong SNe, it is likely that a range of systems of varying sizes and energetics are required to explain Ca-strong SNe. The largest and most energetic of these systems could therefore align with the velocities we observe in for example SN 2022oqm.

The distribution of velocities at peak also gives us insight into the geometry of our progenitor systems. Assuming all Ca-strong SNe originate from broadly uniform progenitor systems, the observed velocity is the projected lobe velocity dependant on the observed inclination of the system. The width of the lobes will determine the distribution of observed velocities, wherein narrow lobes would show very few objects with high velocity [Ca II] and [O I] features, and broader lobes would result in the majority of the [Ca II] and [O I] features having varied, but distinctly non-zero, velocities. The latter of these follows the observed early time distribution across our sample of Ca-strong SNe, indicating that the outflow lobes in our proposed progenitor system are likely broad.

Additionally, as cooling via [O I] emission is relatively inefficient compared to cooling via [Ca II] emission (Jacobson-Galán et al. 2022), to observe the distinct concurrent [O I] and [Ca II] emission across the sample of Ca-strong SNe, we likely required the [Ca II] and [O I] emission to originate from two distinct regions (see section 5.2 of CGTP25). Throughout the spectral evolution of objects in our sample, only five spectra show [O I] emission associated with a 'slower' intrinsic velocity than [Ca II] at the same epoch with a significance level of $>3\sigma$ – in all other cases, the [O I] emission is blueshifted to a greater velocity than the [Ca II]. This supports the stratification of the external environment surrounding the SN, and can be explained by the pre-cursor emission of an AM CVn progenitor.

7.2. Estimation of the 'extended lobe' properties

CGTP25 hypothesise the presence of transition features in spectra with diminishing photospheric features and increasing nebular emission, assumed to start at a phase of ∼14 d. This evolution is what we observe in 22 of the 26 objects with suitable spectra in this key transitional phase. Following our proposed progenitor system, this double-component feature is due to emission from both the lobes and the core of the SN. The presence of two distinct emitting regions at this phase provides us with two key insights into this system. Firstly, at this phase, the photosphere has not yet receded entirely – if this were the case, the [Ca II] feature would be entirely dominated by the zero-velocity intrinsic to the SN core. Secondly, the presence of the high-velocity component in the line profile indicates the SN ejecta have not yet interacted with the [Ca II] emitting region of the lobes. As the emitting region in the lobes is very low density – a requirement to produce the forbidden lines we observe – any interaction between the emitting region of the lobes and the ejecta of the SN itself would disrupt the lobe structure in such a way that its emission would likely no longer be observable.

Therefore, we can infer the minimum size of a lobe in such a system required to reproduce the distinct lobe emission feature we observe in our Ca-strong SN sample. Using the photospheric velocity, latest epoch of observed transition feature, and rise time of the object, we can constrain the minimum physical extension of the emitting lobe. To estimate this, we therefore investigated the object for which we observed both a photospheric spectrum, and the latest possible spectrum with a transitional feature. In our sample of Ca-strong SNe, the object for which these criteria are satisfied is PTF15eqv. This object has a photospheric velocity of 7500 ± 120 km s^{-1} (measured from its He I λ5876 line), and we observe its [Ca II] transitional feature up to +152 d. Combining this with its rise time of 16 d, if we assume homologous expansion, we obtain a lower limit on the lobe size of $1.08 \pm 0.02 \times 10^{16}$ cm. The V445 Puppis system has a physical lobe extension of $1.35 \pm 0.09 \times 10^{17}$ cm (Woudt et al. 2009). The lower limit on the lobe size we would require for similar systems to reproduce the observed behaviour of Ca-strong SNe is therefore physically plausible.

7.3. Early flux excesses from lobe interaction

As discussed in Sect. 5.2, many of the objects in our sample display an observable early flux excess before peak light, consistent with SCE from extended material surrounding the SN progenitor. Under the progenitor channel discussed here, this early flux excess emission is a result of the interaction between the SN shock wave and the polluted environment of the extended lobes of a V445 Puppis-type system. In such a system, the shock wave propagates into the lobes, and the typical SCE scenario progresses from the lobes instead of a traditional spherically symmetric envelope.

As the lobes are not spherically symmetric, the PPBs we observe would therefore also be dependent on the observed angle of each SN event. Observing the system along the pole of the lobes would, theoretically, mean a greater 'radius' (and, assuming a uniform mass distribution both radially and across our sample of Ca-strong objects throughout each lobe, a greater mass) of material shocked along the line of sight; this would, in turn, result in a brighter SCE early flux excess before peak light for any given SN. Conversely, observing the system perpendicular to the lobes would result in minimal shocked material along the line of sight, and therefore, a perhaps imperceptible PPB.

As discussed in Sect. 6 the distribution of velocities of forbidden emission around peak light for any given SN may act as a proxy for the viewing angle of the progenitor system. A high forbidden line velocity at peak indicates we are observing the SN at an angle close to the pole of the lobes, and a low velocity indicates an observation perpendicular to the pole axis. It is therefore reasonable to assume that there would be a correlation between the forbidden emission line velocity at peak, and the SCE radius or mass (again assuming these two quantities are degenerate). We investigated this in Sect. 5.4 and report no such correlation. However, the lack of distinct correlation between early forbidden line emission velocity and physical parameters of extended material surrounding SN progenitors is plausibly driven by the assumption of spherical symmetry in our SCE modelling. The true progenitor system is likely far more complex and asymmetrical (as discussed in Sect. 7.1); thus, these assumptions are over-simplifications. This, combined with the inherent degeneracy between the derived envelope parameters in the Piro (2015) SCE model, results in our derived values of envelope mass and radius serving as estimates on the 'true' values of the environments of each object. It is therefore not a concern for the legitimacy of a V445 Puppis-type progenitor system that we do not observe a clear correlation between the forbidden line velocity at peak light and the radius and mass of the extended environment. We encourage full modelling of this proposed progenitor scenario to fully ascertain whether these predicted correlations are observed.

We argue that the combination of observed photometric and spectroscopic behaviours of Ca-strong SNe across our full sample of objects is in line with the predicted observable signatures of a recurrent He-nova AM CVn system suggested in CGTP25. We can therefore postulate that such systems are responsible for all Ca-strong SNe, uniting the origins of this class of exotic transient, and providing further diagnostic tools in the early classification of future Ca-strong objects.

8. Summary

In this paper we presented optical photometric and spectroscopic observations of the full sample of Ca-strong SNe. Combining literature objects with previously unclassified follow-up targets from the ZTF 2018–2024 sample (and one additional PanSTARRS object) brought our total sample up to 46 objects detected prior to 31 December 2024. Across the sample, we determined the peak brightness and decline rate from all available photometric data. An early-flux excess was distinctly present in 15 of the objects in our sample, and a further 11 objects were consistent with PPBs due to SCE. Across our full sample of 46 confirmed Ca-strong objects, we could not rule out the presence of an early flux excess in any. We investigated correlations between these objects and other observable parameters, but no significant dependencies were apparent.

The core of our investigation focussed on the spectroscopic evolution of our sample, specifically, the evolution of forbidden [Ca II] and [O I] emission lines. Historically, these features have been associated with the nebular phase of these objects, their key diagnostic being a high [Ca II]/[O I] ratio in the nebular-phase. To observe these forbidden transitions we typically assume the photosphere to have receded into the inner layers of the SN, and for the ejecta to have expanded, cooled, and become optically thin, reaching a low enough density for these forbidden transition emission lines to occur. This therefore often requires the SN to be deep in its nebular phase for these features to be observed.

Across our sample of Ca-strong SNe, however, we detect these forbidden emission lines from as early as peak light – far earlier than this typical understanding predicts. To explain the early presence of these features, we investigated the behaviour of the forbidden lines extensively and draw the following conclusions:

- The early presence of [Ca II] and [O I] emission in each object are consistent with the presence of external low-density Ca and O regions that pre-date the SN;
- The broad, non-zero, distribution of velocities in the photospheric phase suggests an extended aspherical external system. Such a system reproduces a broad range of measured velocities dependant on the observed angle of the SN, in line with our observations;
- The narrower, zero-centred velocity distribution of these forbidden lines in the truly nebular-phase spectra of each object may originate from the SN core;
- Investigating higher-resolution spectra observed during transitional epochs reveals a complex line evolution: an initial high-velocity component, which is gradually dominated by a zero-velocity component at later times. This transition is consistent with a shift in the dominant emission region from the external aspherical material at early times, to the inner core at late times as the ejecta expand, become optically thin, and the photosphere recedes entirely;
- Analyses focussing on the early flux excesses observed before peak light in the majority of our sample of Ca-strong SNe indicate that these objects occur in environments that are polluted by pre-existing, extended material.

Our results are consistent with the contribution from two distinct emission regions in the structure of Ca-strong SNe: an external, aspherical structure responsible for early-time forbidden line emission – an interaction which may be responsible for the observed early photometric behaviour of Ca-strong SNe – and a central, core component that dominates in the nebular phase. We therefore hypothesise that Ca-strong SNe result from WD explosions in polluted environments.

We suggest that this pollution may originate from precursor activity of the progenitor itself, such as prior He-novae in AM CVn-based systems. Following our previous work in CGTP25, we suggest that the observed behaviours across the sample of Ca-strong SNe are consistent with the proposed system of a Ca-strong SN progenitor embedded in an environment polluted by an AM CVn recurrent He-nova. In such a scenario, the polar outflow lobes produced by prior nova activity are analogous to the external aspherical structure we conclude is responsible for the photospheric [Ca II] and [O I] emission. The observed emergence of nebular emission would instead be directly produced from the core of the SN itself.

Data availability

The full version of all tables presented in this paper are available at the CDS via https://cdsarc.cds.unistra.fr/viz-bin/cat/J/A+A/714/A262. All ZTF spectra are publicly available through DR2 (https://ztfcosmo.in2p3.fr/), or will become available with the DR3 data release. All spectral data of SN 2021acnz can be found on the ESO archive (https://archive.eso.org). All data is also available upon reasonable request to the author.

Acknowledgements. C.-G.T.-P., K.M., J.H.T. acknowledge funding from Horizon Europe ERC grant no. 101125877. W.J.-G. is supported by NASA through Hubble Fellowship grant HSTHF2-51558.001. M.P. acknowledges support from a UK Research and Innovation Future Leaders Fellowship (grant references MR/T020784/1 and UKRI1062) C.R.A. is supported by the European Research Council (ERC) under the European Union's Horizon 2020 research and innovation program (grant agreement No. 948381, PI: M. Nicholl). C.O.D. acknowledges funding from the Irish Research Council grant no GOIPG/2024/4378. C.L. is supported by DoE award # DE-SC0025599. A.C.G. and the Fong Group at Northwestern acknowledge support by the National Science Foundation under grant Nos. AST-1909358, AST-2206494, AST-2308182 and CAREER grant No. AST-2047919. S.J.S. acknowledges funding from STFC Grants ST/Y001605/1, ST/X001253/1, a Royal Society Research Professorship and the Hintze Family Charitable Foundation. Based on observations obtained with the Samuel Oschin Telescope 48-inch and the 60-inch Telescope at the Palomar Observatory as part of the Zwicky Transient Facility project. ZTF is supported by the National Science Foundation under Grants No. AST-1440341 and AST-2034437 and a collaboration including current partners Caltech, IPAC, the Oskar Klein Center at Stockholm University, the University of Maryland, University of California, Berkeley, the University of Wisconsin at Milwaukee, University of Warwick, Ruhr University Bochum, Cornell University, Northwestern University and Drexel University. Operations are conducted by C.O.O., I.P.A.C., and U.W. SED Machine is based upon work supported by the National Science Foundation under Grant No. 1106171. The ZTF forced-photometry service was funded under the Heising-Simons Foundation grant 12540303 (PI: Graham). The ztfquery code was funded by ERC grant no. 759194 – USNAC, PI: Rigault). W.M. Keck Observatory access was supported by Northwestern University and the Center for Interdisciplinary Exploration and Research in Astrophysics (CIERA). Pan-STARRS is primarily funded to search for near-Earth asteroids through NASA grants NNX08AR22G and NNX14AM74G. The Pan-STARRS science products were made possible through the contributions of the University of Hawai'i Institute for Astronomy, the Queen's University Belfast and the University of Oxford. This work has made use of data from the Asteroid Terrestrial-impact Last Alert System (ATLAS) project. The Asteroid Terrestrial-impact Last Alert System (ATLAS) project is primarily funded to search for near earth asteroids through NASA grants NN12AR55G, 80NSSC18K0284, and 80NSSC18K1575; byproducts of the NEO search include images and catalogues from the survey area. This work was partially funded by Kepler/K2 grant J1944/80NSSC19K0112 and HST GO-15889, and STFC grants ST/T000198/1 and ST/S006109/1. The ATLAS science products have been made possible through the contributions of the University of Hawaii Institute for Astronomy, the Queen's University Belfast, the Space Telescope Science Institute, the South African Astronomical Observatory, and The Millennium Institute of Astrophysics (MAS), Chile and the University of Oxford.

References

Aamer, A., Nicholl, M., Jerkstrand, A., et al. 2024, MNRAS, 527, 11970
Adelman-McCarthy, J. K., Agüeros, M. A., Allam, S. S., et al. 2006, ApJS, 162, 38
Adelman-McCarthy, J. K., Agüeros, M. A., Allam, S. S., et al. 2008, ApJS, 175, 297
Akaike, H. 1974, IEEE Trans. Automatic Control, 19, 716
Alam, S., Albareti, F. D., Allende Prieto, C., et al. 2015, ApJS, 219, 12
Albareti, F. D., Allende Prieto, C., Almeida, A., et al. 2017, ApJS, 233, 25
Allison, J. R., Sadler, E. M., & Meekin, A. M. 2014, MNRAS, 440, 696
Arcavi, I., Hosseinzadeh, G., Brown, P. J., et al. 2017, ApJ, 837, L2
Ayala, B., Anderson, J. P., Pignata, G., et al. 2025, A&A, 701, A128
Baer-Way, R., DeGraw, A., Zheng, W., et al. 2024, ApJ, 964, 172
Bellm, E. C., Kulkarni, S. R., Graham, M. J., et al. 2019, PASP, 131, 018002
Bilicki, M., Jarrett, T. H., Peacock, J. A., Cluver, M. E., & Steward, L. 2014, ApJS, 210, 9
Blondin, S., & Tonry, J. L. 2011, SNID: Supernova Identification, Astrophysics Source Code Library [record ascl:1107.001]
Bose, S., Stritzinger, M. D., Ashall, C., et al. 2025, A&A, 699, A169
Burnham, K. P., & Anderson, D. R. 2004, Sociol. Methods Res., 33, 261
Cabanela, J. E., & Aldering, G. 1998, AJ, 116, 1094
Callan, F. P., Holas, A., Morán-Fraile, J., et al. 2025, A&A, 702, A29
Cappellari, M., Emsellem, E., Krajnović, D., et al. 2011, MNRAS, 413, 813
Cardelli, J. A., Clayton, G. C., & Mathis, J. S. 1989, ApJ, 345, 245
Chambers, K. C., Boer, T. D., Bulger, J., et al. 2023, Transient Name Server Discovery Report, 2023-2518, 1
Chambers, K. C., Magnier, E., Metcalfe, N., et al. 2016, arXiv e-prints [arXiv:1612.05560]
Coughlin, M. W., Bloom, J. S., Nir, G., et al. 2023, ApJS, 267, 31
da Costa, L. N., Willmer, C. N. A., Pellegrini, P. S., et al. 1998, AJ, 116, 1
Dahiwale, A., Fremling, C., & Dugas, A. 2019, Transient Name Server Classification Report, 2019-2097, 1
Das, K. K., Kasliwal, M. M., Fremling, C., et al. 2023, ApJ, 959, 12

Das, K., Covarrubias, S., & Kasliwal, M. 2024, Transient Name Server Classification Report, 2024-3553, 1
De, K. 2021, Transient Name Server Discovery Report, 2021-3269, 1
De, K. 2023, Transient Name Server Discovery Report, 2023-776, 1
De, K., Kasliwal, M. M., Cantwell, T., et al. 2018, ApJ, 866, 72
De, K., Kasliwal, M. M., Tzanidakis, A., et al. 2020, ApJ, 905, 58
De, K., Fremling, U. C., Gal-Yam, A., et al. 2021, ApJ, 907, L18
Dekany, R., Smith, R. M., Riddle, R., et al. 2020, PASP, 132, 038001
DESI Collaboration (Adame, A. G., et al.) 2024, AJ, 168, 58
Dessart, L., & Hillier, D. J. 2015, MNRAS, 447, 1370
Díaz-Giménez, E., Mamon, G. A., Pacheco, M., Mendes de Oliveira, C., & Alonso, M. V. 2012, MNRAS, 426, 296
Dimitriadis, G., Siebert, M. R., Kilpatrick, C. D., et al. 2019, Transient Name Server Classification Report, 2019-675, 1
Dimitriadis, G., Burgaz, U., Deckers, M., et al. 2025, A&A, 694, A10
Dong, Y., Milisavljevic, D., Leja, J., et al. 2022, ApJ, 927, 199
Dong, Y., Milisavljevic, D., Leja, J., et al. 2022, The Journal, 927, 199
Drake, A. J., Djorgovski, S. G., Mahabal, A., et al. 2010, Central Bureau Electron. Telegrams, 2339, 1
Ertini, K., Folatelli, G., Martinez, L., et al. 2023, MNRAS, 526, 279
Falco, E. E., Kurtz, M. J., Geller, M. J., et al. 1999, PASP, 111, 438
Foley, R. J. 2015, MNRAS, 452, 2463
Foreman-Mackey, D., Hogg, D. W., Lang, D., & Goodman, J. 2013, PASP, 125, 306
Forster, F., Bauer, F. E., Pignata, G., et al. 2024, Transient Name Server Discovery Report, 2024-1638, 1
Frohmaier, C., Sullivan, M., Maguire, K., & Nugent, P. 2018, ApJ, 858, 50
Fulton, M., Srivastav, S., & Huber, M. E. 2023, Transient Name Server Classification Report, 2023-2698, 1
Galbany, L., Ashall, C., Höflich, P., et al. 2019, A&A, 630, A76
Graham, M. J., Kulkarni, S. R., Bellm, E. C., et al. 2019, PASP, 131, 078001
Healy, J., Blyth, S.-L., Verheijen, M. A. W., et al. 2021, A&A, 650, A76
Hinkle, J. 2022, Transient Name Server Classification Report, 2022-2170, 1
Hodgkin, S. T., Breedt, E., Delgado, A., et al. 2023, Transient Name Server Discovery Report, 2023-57, 1
Hosseinzadeh, G., Sand, D. J., Valenti, S., et al. 2017, ApJ, 845, L11
Huchra, J. P., Vogeley, M. S., & Geller, M. J. 1999, ApJS, 121, 287
Huchtmeier, W. K., Sage, L. J., & Henkel, C. 1995, A&A, 300, 675
Irani, I., Chen, P., Morag, J., et al. 2024, ApJ, 962, 109
Jacobson-Galán, W. V., Margutti, R., Kilpatrick, C. D., et al. 2020, ApJ, 898, 166
Jacobson-Galán, W. V., Polin, A., Foley, R. J., et al. 2020, ApJ, 896, 165
Jacobson-Galán, W., Venkatraman, P., Margutti, R., et al. 2022, ApJ, 932, 58
Jerkstrand, A. 2017, in Handbook of Supernovae, eds. A. W. Alsabti, & P. Murdin, 795
Johansson, J., Covarrubias, S., Chu, M., & Fremling, C. 2024, Transient Name Server Classification Report, 2024-3029, 1
Jones, D. H., Read, M. A., Saunders, W., et al. 2009, MNRAS, 399, 683
Kasliwal, M. M., Kulkarni, S., Gal-Yam, A., et al. 2012, ApJ, 755, 161
Kass, R. E., & Raftery, A. E. 1995, J. Am. Statist. Assoc., 90, 773
Kato, M., & Hachisu, I. 2003, ApJ, 598, L107
Kawabata, K. S., Maeda, K., Nomoto, K., et al. 2010, Nature, 465, 326
Kawahara, N., Yamanaka, M., Kawabata, K., et al. 2018, in American Astronomical Society Meeting Abstracts, 231, American Astronomical Society Meeting Abstracts #231, 446.03
Lee, G.-H., Hwang, H. S., Sohn, J., & Lee, M. G. 2017, ApJ, 835, 280
Lee, M. G., Jang, I. S., & Kang, J. 2019, ApJ, 871, 33
Lunnan, R., Kasliwal, M. M., Cao, Y., et al. 2017, ApJ, 836, 60
Lunnan, R., Kasliwal, M. M., Cao, Y., et al. 2017, VizieR Online Data Catalog: Bgri light curves of PTF11kmb and PTF12bho (Lunnan+, 2017), VizieR On-line Data Catalog: J/ApJ/836/60. Originally published in: 2017ApJ...836...60L
Lyman, J., Levan, A. J., Church, R., Davies, M. B., & Tanvir, N. 2014, MNRAS, 444, 2157
Maguire, K., Jerkstrand, A., Smartt, S. J., et al. 2012, MNRAS, 420, 3451
Masci, F. J., Laher, R. R., Rusholme, B., et al. 2019, PASP, 131, 018003
Milisavljevic, D., Patnaude, D. J., Raymond, J. C., et al. 2017, ApJ, 846, 50
Morán-Fraile, J., Holas, A., Röpke, F. K., Pakmor, R., & Schneider, F. R. N. 2024, A&A, 683, A44
Mulchaey, J. S., Kasliwal, M. M., & Kollmeier, J. A. 2013, ApJ, 780, L34
Nakaoka, T., Maeda, K., Yamanaka, M., et al. 2021, ApJ, 912, 30
Nakar, E., & Piro, A. L. 2014, ApJ, 788, 193
Nordgren, T. E., Chengalur, J. N., Salpeter, E. E., & Terzian, Y. 1997, AJ, 114, 77
Patterson, M. T., Bellm, E. C., Rusholme, B., et al. 2019, PASP, 131, 018001
Paturel, G., Theureau, G., Bottinelli, L., et al. 2003, A&A, 412, 57
Perets, H. B., Gal-yam, A., Crockett, R. M., et al. 2011, ApJ, 728, L36
Perets, H. B., Gal-Yam, A., Mazzali, P., et al. 2010, Nature, 465, 322
Perets, H. B., Gal-Yam, A., Mazzali, P. A., et al. 2010, Nature, 465, 322
Pessi, T., Prieto, J. L., Monard, B., et al. 2022, ApJ, 928, 138
Petrushevska, T., Ihanec, N., Gromadzki, M., & Yaron, O. 2024, Transient Name Server Classification Report, 2024-110, 1
Piro, A. L. 2015, ApJ, 808, L51
Polin, A., Nugent, P., & Kasen, D. 2019, ApJ, 873, 84
Polin, A., Nugent, P., & Kasen, D. 2021, ApJ, 906, 65
Prentice, S. J., Skillen, K., Maguire, K., Magee, M. R., & Clark, P. 2019, Transient Name Server Classification Report, 2019-336, 1
Prentice, S., Maguire, K., Flörs, A., et al. 2020, A&A, 635, A186
Prentice, S. J., Maguire, K., Boian, I., et al. 2020, MNRAS, 499, 1450
Reguitti, A. 2024, Transient Name Server Classification Report, 2024-3257, 1
Rehemtulla, N., Fremling, C., Perley, D., & Laz, T. D. 2024, Transient Name Server Discovery Report, 2024-3213, 1
Rigault, M., Neill, J. D., Blagorodnova, N., et al. 2019, A&A, 627, A115
Rigault, M., Smith, M., Goobar, A., et al. 2025, A&A, 694, A1
Rines, K. J., Geller, M. J., Diaferio, A., & Hwang, H. S. 2016, ApJ, 819, 63
Roberts, S., Osborne, M., Ebden, M., et al. 2013, Philos. Trans. Roy. Soc. A: Math. Phys. Eng. Sci., 371, 20110550
Roelofs, G. H., Groot, P., Benedict, G., et al. 2007, ApJ, 666, 1174
Sakai, S., Giovanelli, R., & Wegner, G. 1994, AJ, 108, 33
Sanchez-Barrantes, M., Henning, P. A., McIntyre, T., et al. 2019, AJ, 158, 234
Schlafly, E. F., & Finkbeiner, D. P. 2011, ApJ, 737, 103
Schlegel, D. J., Finkbeiner, D. P., & Davis, M. 1998, ApJ, 500, 525
Sell, P. H., Maccarone, T. J., Kotak, R., Knigge, C., & Sand, D. J. 2015, MNRAS, 450, 4198
Sell, P. H., Arur, K., Maccarone, T. J., et al. 2018, MNRAS, 475, L111
Siebert, M. R., Davis, K., Tinyanont, S., Foley, R. J., & Strasburger, E. 2021, Transient Name Server Classification Report, 2021-2383, 1
Smith, K. W., Smartt, S. J., Young, D. R., et al. 2020, PASP, 132, 085002
Sollerman, J., Chu, M., Dahiwale, A., & Fremling, C. 2024a, Transient Name Server Classification Report, 2024-684, 1
Sollerman, J., Fremling, C., Perley, D., & Laz, T. D. 2024b, Transient Name Server Discovery Report, 2024-4282, 1
Springob, C. M., Haynes, M. P., Giovanelli, R., & Kent, B. R. 2005, ApJS, 160, 149
Srivastav, S., Smartt, S. J., Leloudas, G., et al. 2020, ApJ, 892, L24
Srivastav, S., Smartt, S. J., Moore, T., et al. 2026, MNRAS, 549, stag1028
Stone, M. 1979, J. Roy. Stat. Soc. B (Methodological), 276
Sullivan, M., Kasliwal, M. M., Nugent, P. E., et al. 2011, ApJ, 732, 118
Sun, F., & Gal-Yam, A. 2017, arXiv e-prints [arXiv:1707.02543]
Taddia, F., Fremling, C., Sollerman, J., et al. 2016, A&A, 592, A89
Tonry, J., Denneau, L., Heinze, A., et al. 2018, PASP, 130, 064505
Tonry, J., Denneau, L., Heinze, A., et al. 2019, Transient Name Server Discovery Report, 2019-310, 1
Tonry, J., Denneau, L., Weiland, H., et al. 2024, Transient Name Server Discovery Report, 2024-85, 1
Touchard-Paxton, C. G., Frohmaier, C., Pursiainen, M., et al. 2025, MNRAS, 537, 1015
Valenti, S., Benetti, S., Cappellaro, E., et al. 2008, MNRAS, 383, 1485
Valenti, S., Yuan, F., Taubenberger, S., et al. 2014, MNRAS, 437, 1519
van den Bosch, R. C. E., Gebhardt, K., Gültekin, K., Yıldırım, A., & Walsh, J. L. 2015, ApJS, 218, 10
van der Walt, S., Crellin-Quick, A., & Bloom, J. 2019, J. Open Source Softw., 4, 1247
van Driel, W., Butcher, Z., Schneider, S., et al. 2016, A&A, 595, A118
Waldman, R., Sauer, D., Livne, E., et al. 2011, ApJ, 738, 21
Wang, L.-L., Luo, A.-L., Shen, S.-Y., et al. 2018, MNRAS, 474, 1873
Williams, C. K. I., & Rasmussen, C. E. 2006, Gaussian Processes for Machine Learning (Cambridge, MA: MIT Press)
Wong, O. I., Ryan-Weber, E. V., Garcia-Appadoo, D. A., et al. 2006, MNRAS, 371, 1855
Woudt, P., Steeghs, D., Karovska, M., et al. 2009, ApJ, 706, 738
Zenati, Y., Perets, H. B., Dessart, L., et al. 2023, ApJ, 944, 22

Appendix A: Reclassifications of literature transients

Das et al. (2023) presented a sample of 'IIb-Ca-strong' objects – objects with a high [Ca II]/[O I] ratio at late-times, but with broad H features in the photospheric spectra akin to Type IIb SNe. Our analysis of the photospheric spectra of these objects, however, indicates the features previously identified as H in several of these objects would require unphysical velocities, with the absorption occurring at 0 km s^{-1}. The velocities of these features among this subsample of 'IIb-Ca-strong' objects are consistent with the expected velocities of He I at these phases. Additionally, if this were He I, the required velocity for this observed feature is consistent across each feature in the He I λ4471, λ5876, λ6678, λ7065 series, further indicating the chemical species responsible for this feature to be He I. Due to this, we update the classification of SN 2019ehk, SN 2019pof, and SN 2021sjt (Ayala et al. 2025; Jacobson-Galán et al. 2020; Nakaoka et al. 2021; Siebert et al. 2021; Dahiwale et al. 2019; Das et al. 2023; Dimitriadis et al. 2019) and include them in our sample of 'confirmed' Ca-strong objects.

We reclassify five candidate Ca-strong SNe from De et al. (2020) for the following reasons:

SN 2019txr (SN Ib/c): the +270d spectrum, from which the De et al. (2020) [Ca II]/[O I] ratio was determined, is host-dominated and has a very low S/N; we did not clearly identify any distinct features in this spectrum. We instead obtain our [Ca II]/[O I] value from the +30d spectrum ([Ca II]/[O I]=> 2.21), a phase consistent with our definition of the nebular phase. As this value meets Criterion 4 of our classification requirements, we include SN 2019txr as a Ca-strong object.

SN 2019ouq (SN Ic): Fitting the [Ca II] and [O I] features of the +180d spectrum with the methodology described in 4, we obtain a [Ca II]/[O I] ratio of 3.62. As this is above the threshold value of 2 (see Criterion 4), we therefore include SN 2019ouq in our sample.

SN 2018kqr (SN Ic-BL): The spectrum at +14d is still in the transitional-phase between the photospheric and nebular regimes. De et al. (2020) describe this object as having slow photospheric-phase evolution, but without later spectra (or a better-constrained value on its photometric decline rate, Δm_7; see Sect. 3) we cannot comfortably come to the same conclusion. We therefore continue to treat this object as a Ca-strong SN as it satisfies each of our classification criteria.

SN 2019gau (SN Ia): While the only late-time spectrum of this object (+250d) is contaminated by host emission, we tentatively identify a [Ca II] feature. As this spectrum is so dominated by host emission, and we cannot concretely confirm the presence of [Ca II], we treated this object as though its latest-available spectrum was the previous spectrum, at +9d, and proceeded with its classification under this assumption. Its spectrum at this epoch resembled that of other confirmed Ca-strong objects, and its photometric properties are in line with the rest of the sample, so we continued to assume SN 2019gau to be a Ca-strong object.

SN 2018dbg (SN Ib/c): The only spectrum available (+28d) contains distinct NIR triplet, [Ca II], and [O I] emission. Additionally, the photometric behaviour (M_{peak}, Δm_7, $g-r$ colour) of this object was in line with the rest of the sample. We therefore proceeded with our classification of SN 2018dbg as a member of our full Ca-strong sample.

Appendix B: Additional plots and tables

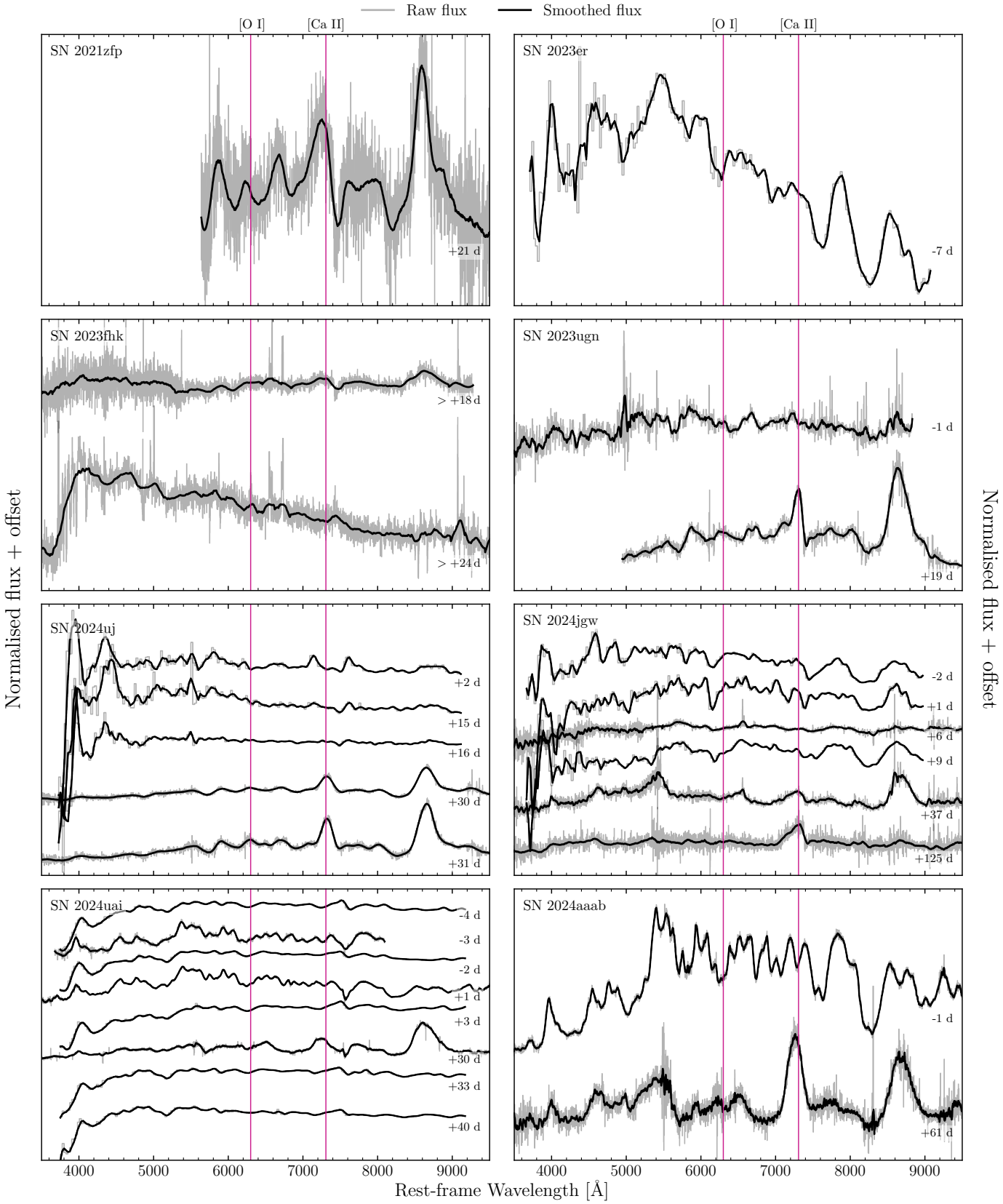


Fig. B.1. Spectral time series for each of the eight confirmed new Ca-strong SNe in our sample. Each spectrum (light grey) is overlaid with a Savitzky-Golay smoothed spectrum (black). The rest-frame phase relative to *r*-band peak of each spectroscopic observation is labelled. Any narrow host emission lines present in the spectra, namely for objects SN 2022psx and SN 2023fhk, are masked from the spectra to ensure consistent scaling of the SN spectral emission between epochs and across objects. The vertical pink lines correspond to the weighted mean wavelength values of the [O I] $\lambda\lambda$6300,6364 and [Ca II] $\lambda\lambda$7291,7324 features, respectively, based on their relative component line intensities.

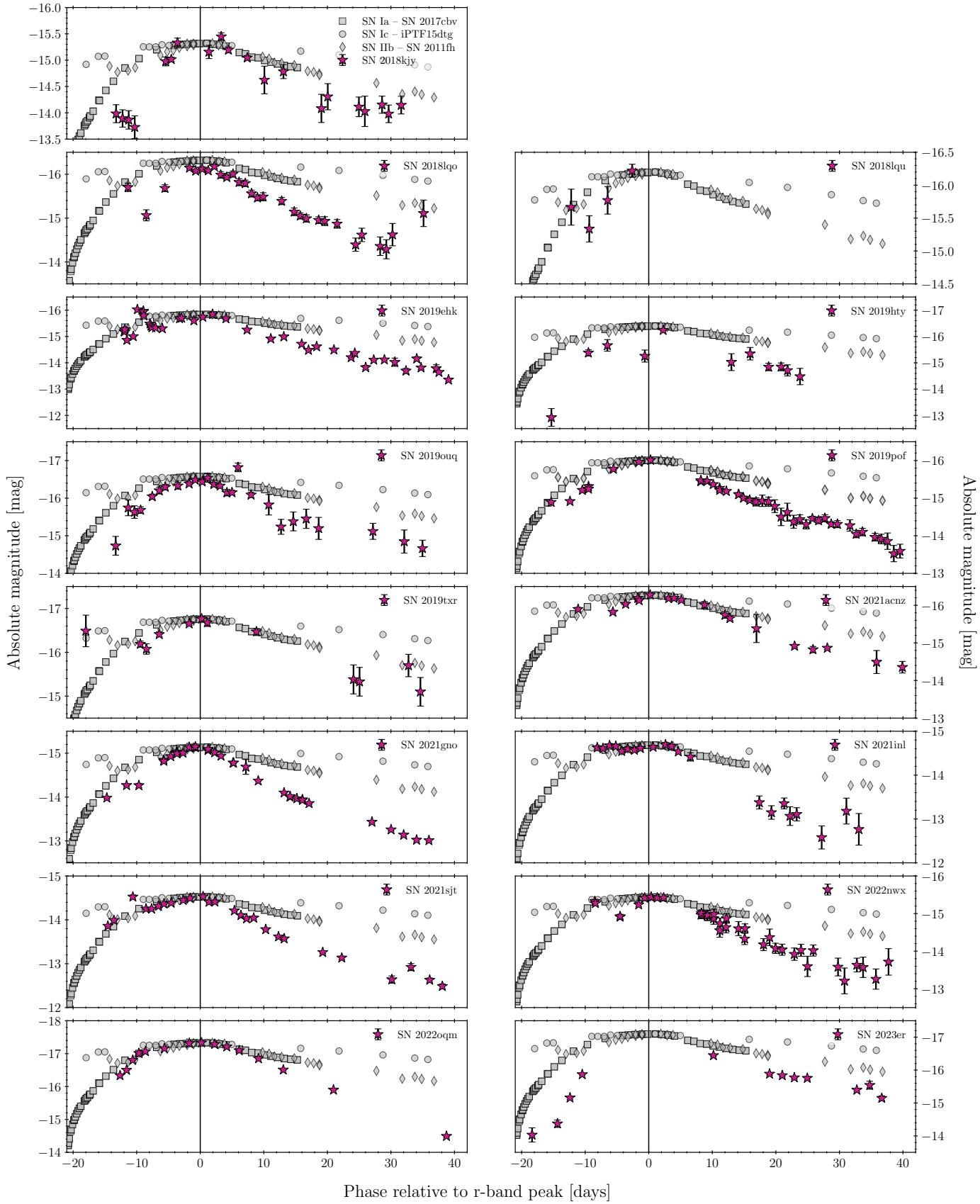


Fig. B.2. *r*-band light curves of the 15 objects in our sample with confirmed early flux excesses. Each object (labelled in the subplot; left to right, top to bottom: SN 2018kjy, SN 2018lqo, SN 2018lqu, SN 2019ehk, SN 2019hty, SN 2019ouq, SN 2019pof, SN 2019txr, SN 2021acnz, SN 2021gno, SN 2021inl, SN 2021sjt, SN 2022nwx, SN 2022oqm, and SN 2023er) is plotted against the light curves of known SNe with PPBs – SN Ia (SN 2017cbv, squares), SN Ic (iPTF15dtg, circles), and SN IIb (SN 2011fh, diamonds) – scaled to the peak brightness of that object.

Table B.1. Key physical properties of all Ca-strong SN candidates.

	IAU Name	ZTF Name	Host	z	E(B-V) [Mag]	R_{off} [kpc]	[Ca II]/[O I]	Reference
Confirmed Ca-strong	SN 2000ds		NGC 2768	0.004513 ± 0.0000170	0.0374 ± 0.0020	3.54 ± 0.39	†	1, 2, 3
	SN 2001co		NGC 5559	0.017175 ± 0.00000973	0.0169 ± 0.0002	6.91 ± 0.20	≥ 2.51	4, 2, 3
	SN 2003H		NGC 2207	0.009176 ± 0.00000200	0.0748 ± 0.0006	10.59 ± 0.57	4.48 ± 0.12	5, 2, 3
	SN 2003dg		UGC 6934	0.018339 ± 0.00000700	0.0205 ± 0.0016	1.22 ± 0.03	7.89 ± 0.09	6, 2, 3
	SN 2003dr		NGC 5714	0.007472 ± 0.00000500	0.0125 ± 0.0009	2.46 ± 0.16	7.62 ± 0.14	5, 2, 3
	SN 2005E		NGC 1032	0.009150 ± 0.0000120	0.0315 ± 0.0012	26.37 ± 1.47	6.67 ± 0.09	5, 7, 8, 9, 3
	SN 2005cz		NGC 4589	0.006605 ± 0.0000467	0.0241 ± 0.0006	6.06 ± 0.45	11.20 ± 0.08	10, 8, 11, 2, 3
	SN 2007ke		NGC 1129	0.017472 ± 0.0000470	0.0949 ± 0.0039	22.28 ± 0.63	†	12, 2, 3
	PTF09dav		2MASX J22465295+2138221	0.037100 ± 0.000200	0.0398 ± 0.0005	45.05 ± 0.61	≥ 4.37	13, 13, 14, 2, 3
	SN 2010et		SDSS J171650.20+313234.4	0.023461 ± 0.0000132	0.0366 ± 0.0009	48.21 ± 1.03	14.83 ± 0.03	4, 15, 2, 3
	PTF11kmb		NGC 7265	0.016661 ± 0.0000477	0.0905 ± 0.0021	174.08 ± 5.15	10.18 ± 0.10	12, 2, 16, 3
	PTF12bho		LEDA 44863	0.023430 ± 0.0000100	0.0080 ± 0.0004	56.45 ± 1.20	12.37 ± 0.07	17, 18, 16, 3
	PTF15eqv		NGC 3430	0.005290 ± 0.00000300	0.0201 ± 0.0002	4.89 ± 0.53	5.07 ± 0.07	19, 20, 3, 21
	SN 2016hgs		2MASX J00505254+2722432	0.017000	0.0528 ± 0.0018	6.38 ± 0.19	7.09 ± 0.07	22, 3, 23
	SN 2016hnk		MCG-01-06-070	0.015942 ± 0.00000700	0.0224 ± 0.0008	4.23 ± 0.13	≥ 6.82	24, 25, 3, 26, 27
	SN 2018ckd	ZTF18aayhylv	NGC 5463	0.023649 ± 0.0000477	0.0243 ± 0.0004	19.55 ± 0.41	4.16 ± 0.02	12, 3
	SN 2018dbg	ZTF18abdffeo	IC 4397	0.014744 ± 0.0000200	0.0174 ± 0.0004	0.65 ± 0.02	†	28, 3
	SN 2018gwo	ZTF18acbwazl	NGC 4128	0.007442 ± 0.000051	0.0187 ± 0.0006	16.46 ± 0.01	5.65 ± 0.07	12, 3
	SN 2018kjy	ZTF18acsodbf	NGC 2256	0.017519 ± 0.000193	0.1125 ± 0.0016	28.89 ± 0.94	2.97 ± 0.62	6, 3
	SN 2018kqr	ZTF18acushie	SDSS J085003.97+551010.1	0.04425 ± 0.00001	0.0293 ± 0.0016	5.07 ± 0.06	†	29, 3
	SN 2018lqo	ZTF18abmxelh	Z 224-43	0.032280 ± 0.00000900	0.0059 ± 0.0004	18.91 ± 0.29	12.19 ± 0.08	24, 3
	SN 2018lqu	ZTF18abttsrb	WISEA J155413.91+133102.4	0.034826 ± 0.0000231	0.0359 ± 0.0007	28.42 ± 0.40	3.93 ± 0.06	4, 3
	SN 2019bkc		NGC 3090	0.020311 ± 0.0000670	0.0453 ± 0.0035	91.97 ± 2.26	†	30, 31, 32, 33
	SN 2019ehk	ZTF19aatesgp	M 100	0.005240 ± 0.00000300	0.0227 ± 0.0002	2.44 ± 0.23	≥ 3.42	34, 35, 36, 37, 38
	SN 2019gau	ZTF19aavlfvn	2MASS J14381034+1008062	0.027683 ± 0.0000131	0.0261 ± 0.0006	0.80 ± 0.01	†	4, 3
	SN 2019hty	ZTF19aaznwze	WISEA J125534.50+321221.5	0.022829 ± 0.00000676	0.0141 ± 0.0008	9.20 ± 0.19	2.33 ± 0.03	39, 3
	SN 2019ofm	ZTF19abrdxbh	IC 4514	0.030254 ± 0.0000106	0.0248 ± 0.0014	11.96 ± 0.20	4.89 ± 0.04	4, 3
	SN 2019ouq	ZTF19abhhdwf	LEDA 1890714	0.035864 ± 0.0000247	0.0259 ± 0.0004	7.71 ± 0.11	3.62 ± 0.02	4, 3
	SN 2019pof	ZTF19abxtcio	PSO J018.1606+33.0353	0.0155	0.0508 ± 0.0008	3.21 ± 0.11	≥ 5.21	40, 37
	SN 2019pxu	ZTF19abwtqsk	LEDA 147063	0.028200 ± 0.000150	0.1026 ± 0.0035	18.13 ± 0.44	4.29 ± 0.32	41, 3
	SN 2019txr	ZTF19aarrdoz	LEDA 2532103	0.044433	0.0337 ± 0.0026	3.26 ± 0.04	≥ 2.21	42, 3
	SN 2021gno	ZTF21aaqhhfu	NGC 4165	0.006231 ± 0.0000157	0.0295 ± 0.0013	3.21 ± 0.26	†	4, 43, 3
	SN 2021inl	ZTF21aasuego	NGC 4923	0.018257 ± 0.00000659	0.0077 ± 0.0004	22.79 ± 0.63	†	44, 43
	SN 2021sjt	ZTF21abjyiiw	NGC 6951	0.004750 ± 0.00000334	0.3178 ± 0.0086	7.54 ± 0.79	†	45, 37
	AT 2021zfp	ZTF21acddxti	2MASX J10133383+3842365	0.023034 ± 0.00000700	0.0111 ± 0.0002	13.12 ± 0.28	†	46, 47
	SN 2021acnz	ZTF21aciwixf	NGC 165	0.019644 ± 0.00000667	0.0296 ± 0.0002	40.38 ± 1.11	7.33 ± 0.01	48, 49
	SN 2022nwx	ZTF22aapisdk	NGC 7242	0.019304 ± 0.0000407	0.1289 ± 0.0021	37.87 ± 0.99	7.81 ± 0.05	12
	SN 2022oqm	ZTF22aasxgjp	NGC 5875	0.011695 ± 0.000007	0.0164 ± 0.0005	18.44 ± 0.82	6.90 ± 0.04	50, 51
	SN 2023er	ZTF22abyrurb	2MASX J01021072+3224501	0.016285 ± 0.0000870	0.0653 ± 0.0010	123.15 ± 3.68	†	52, 53, 54
	SN 2023fhk	ZTF23aaawmyi	2MASX J22301302+3703304	0.024200	0.1067 ± 0.0019	0.57 ± 0.23	†	55, 56, 57
	SN 2023ugn		NGC 915	0.03224 ± 0.00008 ‡	0.0894 ± 0.0047	13.02 ± 0.22	†	6, 58, 59
	SN 2023xwi	ZTF23abrgldj	PSO J146.8867+71.243	0.0112 ± 0.0005	0.0557 ± 0.0026	9.12 ± 0.41	23.02 ± 0.02	60
	SN 2024uj	ZTF24aabuxza	NGC 3565	0.012612 ± 0.000130	0.0423 ± 0.0024	5.93 ± 0.24	4.57 ± 0.07	61, 62, 63

Continued on next page

Table B.1. Continued from previous page

	IAU Name	ZTF Name	Host	z	E(B-V) [Mag]	R_{off} [kpc]	[Ca II]/[O I]	Reference
	SN 2024jgw	ZTF24aaosvzx	WISEA J171503.17+460243.5	0.028 *	0.0302 ± 0.0009	2.86 ± 0.05	†	64, 65
	SN 2024uai	ZTF24abejmqz	NGC 2300	0.006354 ± 0.0000230	0.0815 ± 0.0043	3.45 ± 0.29	5.07 ± 0.09	66, 67, 68
	AT 2024aaab	ZTF24abpgriz	Z 307-16	0.017359 ± 0.000160	0.2296 ± 0.0123	19.04 ± 0.55	≥ 3.76	6, 69
Not Ca-strong	SN 2012hn		NGC 2272	0.007104 ± 0.0000320	0.0833 ± 0.0039	–	1.63 ± 0.19	70, 71, 2, 3
	SN 2018fob	ZTF18aboabxv	NGC 5888	0.029050 ± 0.0000110	0.0178 ± 0.0020	–	0.49 ± 0.03	4, 3
	SN 2019ttf	ZTF19abalbim	Z 143-17	0.011221 ± 0.0000113	0.1276 ± 0.0031	2.81 ± 0.12	†	72, 3
	SN 2019gsc	ZTF19aawhlcn	Z 273-16	0.011299 ± 0.0000113	0.0081 ± 0.0003	4.10 ± 0.18	2.51 ± 0.02	4, 3
	SN 2018gjx	ZTF18abwkrbl	NGC 865	0.009990 ± 0.00000500	0.0758 ± 0.0009	–	3.01 ± 0.09	5, 73, 3, 37
	SN 2018jak	ZTF18acqxyiq	LEDA 2056276	0.038491 ± 0.0000102	0.0105 ± 0.0004	–	1.01 ± 0.04	4, 3, 37
	SN 2019yz	ZTF19aadttht	UGC 9977	0.006388 ± 0.00000900	0.0949 ± 0.0022	–	0.50 ± 0.02	5, 3
	SN 2019abb	ZTF19aadwtoe	Z 58-66	0.015295 ± 0.00000600	0.0323 ± 0.0016	–	0.41 ± 0.04	74, 3
	SN 2019ape	ZTF19aailcgs	NGC 3426	0.020305 ± 0.00000751	0.0302 ± 0.0006	–	1.29 ± 0.03	4, 3
	SN 2019ccm	ZTF19aamfupk	UGC 3110	0.014947 ± 0.0000170	0.140 ± 0.006	–	1.05 ± 0.01	5
	SN 2019mjo	ZTF19abgqruu	MCG+00-01-026	0.042196 *	0.018 ± 0.007	–	1.42 ± 0.04	75, 3
	SN 2019txl	ZTF19aanfsmc	UGC 5084	0.033806 ± 0.00000969	0.018 ± 0.008	–	0.54 ± 0.01	4, 3
	SN 2019txt	ZTF19aasqseq	IC 583	0.026391 ± 0.00000886	0.029 ± 0.009	–	0.39 ± 0.04	4, 3
	SN 2019weu	ZTF19acxgxcu	WISEA J232432.49+050638.5	0.038 *	0.048 ± 0.007	–	†	3
	SN 2020sbw	ZTF20abwzqzo	CGCG 389-007	0.022769 ± 0.00000900	0.0325 ± 0.0007	–	8.06 ± 0.07	5, 37
	SN 2021M		UGC 9113	0.010624 ± 0.0000149	0.0197 ± 0.0012	–	6.87 ± 0.07	4, 37
	SN 2021pb	ZTF21aabxjqr	2MASX J09444707+5141192	0.033178 ± 0.0000117	0.0088 ± 0.0009	–	1.27 ± 0.15	4, 37
	AT 2021niv	ZTF21abmkuji	LEDA 1102966	0.018419 ± 0.000150	0.032 ± 0.005	–	†	41, 3
	SN 2022psx	ZTF22aawcmcr	WISEA J230439.90+372359.9	0.019 *	0.137 ± 0.002	–	7.51 ± 0.03	76
	SN 2022sfh	ZTF22abdgnuc	2MASX J02365426+3752234	0.032452 ± 0.0000930	0.045 ± 0.004	–	13.28 ± 0.09	77

IAU name, ZTF name, host galaxy, redshift, extinction magnitude, projected offset from host galaxy, [Ca II]/[OI] ratio, and associated references are presented. Confirmed and rejected Ca-strong objects from the full sample of candidates are labelled accordingly. Objects SN 2019gsc (Srivastav et al. 2020) and SN 2019ttf were previously classified as SNe Iax and exhibit strong matches with this SN class around peak; we therefore exclude them from our sample. Objects with redshift values marked with an asterisk (*) have no available uncertainties. The redshift of SN 2023ugn – denoted with a dagger (‡) – has been separately reported with two different values: 0.03224 ± 0.00008 and 0.014673 ± 0.000067. Based on the observed wavelength of the Ca II NIR triplet in the latest spectrum of this object, we use a redshift value of 0.03224 ± 0.00008. Object [Ca II]/[O I] values marked with a double dagger (†) have no spectroscopic observations after +30 d, and as such their nebular [Ca II]/[O I] ratio could not be measured. Objects with upper limits of this value presented have [O I] emission of S/N<3 in their latest available epoch.

1. Cappellari et al. (2011)
2. Foley (2015)
3. De et al. (2020)
4. Albareti et al. (2017)
5. Springob et al. (2005)
6. Falco et al. (1999)
7. Perets et al. (2010)
8. Kawabata et al. (2010)
9. Waldman et al. (2011)
10. Lee et al. (2019)
11. Perets et al. (2011)
12. van den Bosch et al. (2015)
13. Sullivan et al. (2011)
14. Kasliwal et al. (2012)
15. Drake et al. (2010)
16. Lunnan et al. (2017)
17. Healy et al. (2021)
18. Lunnan et al. (2017)
19. Nordgren et al. (1997)
20. Milisavljevic et al. (2017)
21. Kawahara et al. (2018)
22. Dong et al. (2022)
23. De et al. (2018)
24. Lee et al. (2017)
25. Galbany et al. (2019)
26. Sell et al. (2018)
27. Jacobson-Galán et al. (2020)
28. Paturel et al. (2003)
29. Alam et al. (2015)
30. Tonry et al. (2019)
31. Prentice et al. (2019)
32. Huchtmeier et al. (1995)
33. Prentice et al. (2020)
34. Allison et al. (2014)
35. Jacobson-Galán et al. (2020)
36. Nakaoka et al. (2021)
37. Das et al. (2023)
38. De et al. (2021)
39. Rines et al. (2016)
40. Ayala et al. (2025)
41. Jones et al. (2009)
42. Wang et al. (2018)
43. Jacobson-Galán et al. (2022)
44. DESI Collaboration (2024)
45. Baer-Way et al. (2024)
46. Adelman-McCarthy et al. (2006)
47. De (2021)
48. van Driel et al. (2016)
49. Frohmaier+ in prep.
50. van Driel et al. (2016)
51. Irani et al. (2024)
52. Sakai et al. (1994)
53. Hodgkin et al. (2023)
54. Sollerman et al. (2024a)
55. Cabanela & Aldering (1998)
56. De (2023)
57. Das et al. (2024)
58. Chambers et al. (2023)
59. Fulton et al. (2023)
60. Touchard-Paxton et al. (2025)
61. da Costa et al. (1998)
62. Tonry et al. (2024)
63. Petrushevska et al. (2024)
64. Forster et al. (2024)
65. Johansson et al. (2024)
66. Díaz-Giménez et al. (2012)
67. Rehemtulla et al. (2024)
68. Reguitti (2024)
69. Sollerman et al. (2024b)
70. Wong et al. (2006)
71. Sell et al. (2015)
72. Sanchez-Barrantes et al. (2019)
73. Prentice et al. (2020)
74. Adelman-McCarthy et al. (2008)
75. Bilicki et al. (2014)
76. Hinkle (2022)
77. Huchra et al. (1999)

Table B.2. Optical spectroscopy of the eight newly confirmed Ca-strong objects.

Object	MJD	Phase [days]	Telescope	Instrument
SN 2021zfp	59482	+3	Keck II	NIRES
	59500	+21	P200	DBSP
SN 2023er	59940	−7	P60	SEDm*
SN 2023fhk	60054	≥+18	P200	DBSP
	60060	≥+24	Keck I	LRIS
SN 2023ugn	60231	−1	UH88	SNIFS
	60251	+19	–	–
SN 2024uj	60326	+2	P60	SEDm*
	60339	+15	P60	SEDm*
	60340	+16	P60	SEDm*
	60354	+30	Keck I	LRIS
	60355	+31	P60	SEDm*
SN 2024jgw	60461	-2	P60	SEDm*
	60464	+1	P60	SEDm*
	60468	+6	Lick	KAST
	60472	+9	P60	SEDm*
	60500	+37	P200	DBSP
	60588	+125	Keck I	LRIS
SN 2024uai	60554	-4	P60	SEDm*
	60555	-3	Copernico 1.82m	AFOSC
	60556	-2	P60	SEDm*
	60559	+1	NOT	ALFOSC
	60561	+3	P60	SEDm*
	60588	+30	Keck I	LRIS
	60591	+33	P60	SEDm*
	60598	+40	P60	SEDm*
SN 2024aaab	60380	−1	Keck I	LRIS
	60707	+61	Keck I	LRIS

Notes. *SEDm spectra obtained with the Spectral Energy Distribution Machine (Rigault et al. 2019).

Table B.3. Photometric parameters of the confirmed Ca-strong SNe.

Object	MJD_{peak}	M_{peak} (r) [mag]	$\Delta m_7(r)$ [mag]	$g-r$ colour [mag]
SN 2000ds	51827.0 [†, 1]	–	–	–
SN 2001co	52013.0 [†, 1]	–	–	–
SN 2003H	52599.0 [†, 1]	–	–	–
SN 2003dg	52749.0 [†, 1]	–	–	–
SN 2003dr	52779.0 [†, 1]	–	–	–
SN 2005E	53377.0 [†, 2]	–	–	–
SN 2005cz	53691.0 [†, 3]	–	–	–
SN 2007ke	54369.5 [†, 1]	–	–	–
PTF09dav	55054.5 ± 0.3	−16.09 ± 0.04	0.38 ± 0.07	0.38 ± 0.08
SN 2010et	55359.4 [†, 4]	–	–	–
PTF11kmb	55800.7 ± 0.2	−15.64 ± 0.01	0.32 ± 0.01	0.32 ± 0.02
PTF12bho	55992.7 ± 0.2	−16.15 ± 0.04	0.54 ± 0.05	0.54 ± 0.06
PTF15eqv	57363.0 [†, 5]	–	–	–
SN 2016hgs	57692.5 ± 0.3	−15.67 ± 0.03	0.53 ± 0.03	0.85 ± 0.04
SN 2016hnk	57694.5 ± 0.4	−16.99 ± 0.01	0.37 ± 0.02	1.28 ± 0.02
SN 2018ckd	58277.8 ± 0.3	−15.88 ± 0.02	0.47 ± 0.03	0.89 ± 0.04
SN 2018dbg	58307.0 ± 0.1	−16.51 ± 0.02	0.28 ± 0.03	0.88 ± 0.04
SN 2018gwo	58392.0 [†, 6]	–	–	–
SN 2018kjy	58461.9 ± 0.3	−15.32 ± 0.04	0.30 ± 0.05	0.30 ± 0.05
SN 2018kqr	58466.9 ± 0.2	−16.66 ± 0.03	0.14 ± 0.03	0.78 ± 0.04
SN 2018lqo	58352.3 ± 0.1	−16.14 ± 0.02	0.46 ± 0.03	0.45 ± 0.06
SN 2018lqu	58370.8 [†, 6]	–	–	–
SN 2019bkc	58546.98 ± 0.1	−17.34 ± 0.03	2.16 ± 0.12	0.14 ± 0.02
SN 2019ehk	58615.2 ± 0.02	−15.45 ± 0.05	0.38 ± 0.03	1.54 ± 0.06
SN 2019gau	58630.0 [†, 6]	–	–	–
SN 2019hty	58657.9 [†, 6]	–	–	–
SN 2019ofm	58723.6 [†, 6]	–	–	–
SN 2019ouq	58692.0 [†, 6]	–	–	–
SN 2019pof	58748.4 ± 0.3	−16.01 ± 0.01	0.39 ± 0.01	0.50 ± 0.01
SN 2019pxu	58747.8 [†, 6]	–	–	–
SN 2019txr	58610.4 ± 0.4	−16.76 ± 0.04	0.29 ± 0.05	1.10 ± 0.04
AT 2021zfp	≥59479.0	–	–	–
SN 2021acnz	59527.0 ± 0.1	−16.27 ± 0.01	0.30 ± 0.02	0.50 ± 0.02
SN 2021gno	59307.2 ± 0.0	−15.14 ± 0.01	0.46 ± 0.01	0.50 ± 0.01
SN 2021inl	59320.7 ± 0.2	−14.69 ± 0.02	0.82 ± 0.02	0.72 ± 0.02
SN 2021sjt	59416.6 ± 0.1	−14.53 ± 0.01	0.44 ± 0.02	1.64 ± 0.02
SN 2022nwx	59765.7 ± 0.2	−15.43 ± 0.03	0.47 ± 0.04	0.68 ± 0.03
SN 2022oqm	59785.1 ± 0.3	−17.33 ± 0.01	0.30 ± 0.01	0.46 ± 0.02
SN 2023er	59937.0 ± 0.2	−17.29 ± 0.03	0.42 ± 0.01	0.47 ± 0.06
SN 2023fhk	≥60036.0	–	–	–
SN 2023ugn	60232.0 ± 2.3	–	–	–
SN 2023xwi	60274.9 ± 0.1 [†, 7]	−16.8 ± 0.01	–	–
AT 2024aaab	60617.0 ± 0.2	−16.64 ± 0.01	0.32 ± 0.03	1.63 ± 0.03
SN 2024jgw	60463.1 ± 0.1	−17.26 ± 0.01	0.53 ± 0.02	0.89 ± 0.01
SN 2024uai	60560.8 ± 0.4	−16.52 ± 0.02	0.51 ± 0.03	1.02 ± 0.02
SN 2024uj	60324.0 ± 1.4	–	–	–

Notes. MJD of peak r-band light, peak r-band magnitude and associated error, the decline rate (Δ_{m_7}(r)), and the $g-r$ colour at peak of each object in our sample of confirmed Ca-strong objects. Of the full sample, ten objects do not have photometric coverage around peak light: SN 2000ds, SN 2001co, SN 2003H, SN 2003dg, SN 2005E, iPTF15eqv, SN 2018gwo, SN 2018lqu, SN 2023fhk, and SN 2024uj. Values and associated uncertainties for objects with photometric properties determined using GP fitting are listed. Objects with peak light times (and where possible, peak r-band magnitudes) from their associated publications are labelled with a dagger (†) and the appropriate citation (see footnote). The peak light time for objects AT 2021zfp, SN 2023fhk, SN 2023ugn, and SN 2024uj were determined through comparison with other Ca-strong objects.

1. Kasliwal et al. (2012)
2. Perets et al. (2010)
3. Kawabata et al. (2010)
4. Foley (2015)
5. Milisavljevic et al. (2017)
6. De et al. (2020)
7. Touchard-Paxton et al. (2025)

Table B.4. ΔAIC and ΔBIC statistics for fitting the transitional spectroscopic features.

Object	Phase [d]	ΔAIC	ΔBIC
SN 2000ds	14.0	−14.37	−4.83
SN 2003H	99.0	−8.91	−2.01
SN 2003dg	70.0	−16.81	−6.61
SN 2003dr	40.0	−15.74	−6.09
SN 2005E	18.3	−14.59	−8.40
	51.3	−13.33	−6.15
SN 2005cz	40.0	−11.68	−1.65
PTF09dav	13.6	−11.75	−4.28
	91.6	−8.96	−2.72
SN 2010et	84.6	−13.12	−1.68
PTF11kmb	24.3	−8.95	−2.71
PTF12bho	14.0	−22.72	−11.05
	17.0	−20.30	−8.98
	52.0	−15.18	−7.08
PTF15eqv	24.0	−17.36	−7.25
	42.0	−20.87	−9.91
	70.0	−17.92	−7.97
	86.0	−17.40	−8.06
	129.0	−15.07	−4.35
	152.0	−15.88	−4.06
SN 2016hgs	28.2	−8.77	−3.32
	58.2	−13.77	−3.41
SN 2018ckd	59.3	−12.69	−2.50
SN 2018gwo	157.0	−16.80	−5.96
SN 2018kjy	26.1	−24.84	−12.82
	115.1	−17.34	−5.74
SN 2018kqr	14.0	−4.04	−9.02
SN 2018lqo	51.1	−12.43	−3.62
SN 2018lqu	32.2	−15.04	−4.33
SN 2019ofm	173.4	−5.60	0.48
SN 2019pof	149.0	−14.57	−3.19
AT 2021zfp	21.0	−4.83	−2.57
SN 2022nwx	17.0	−12.85	−4.14
	30.0	−20.62	−10.37
	78.0	−16.39	−5.18
SN 2022oqm	26.0	−9.53	−1.25
	60.0	−13.29	−3.45
SN 2023xwi	13.1	−11.90	−4.44
	30.1	−10.80	−3.33
	86.1	−17.81	−9.32
SN 2024uj	30.0	−16.78	−5.56
	31.0	−15.43	−4.52
SN 2024uai	30.0	−18.56	−6.88

Notes. Differences in ΔAIC and ΔBIC between double- and single-component Gaussian models are provided. Negative values indicate a preference for the double-component model. $|\Delta AIC| \geq 5$ and $|\Delta BIC| \geq 2$ indicates a strong preference for the double-component model.

Table B.5. Pre-peak light curve modelling parameters.

SN	Type	M_e [$M_\odot$]	R_e [$R_\odot$]
SN 2018kjy	Present	$0.029^{+0.012}_{-0.013}$	24^{+12}_{-6}
SN 2018lqo	Present	$0.173^{+0.080}_{-0.096}$	186^{+47}_{-33}
SN 2018lqu	Present	$0.264^{+0.063}_{-0.093}$	278^{+99}_{-89}
SN 2019ehk	Present	$0.006^{+0.001}_{-0.001}$	146^{+22}_{-22}
SN 2019hty	Present	$0.40^{+0.17}_{-0.06}$	216^{+36}_{-27}
SN 2019ouq	Present	$0.054^{+0.059}_{-0.021}$	179^{+39}_{-18}
SN 2019pof	Present	$0.0196^{+0.0011}_{-0.0010}$	111^{+16}_{-16}
SN 2019txr	Present	$0.159^{+0.053}_{-0.072}$	339^{+72}_{-48}
SN 2021gno	Present	$0.0405^{+0.0025}_{-0.0023}$	$58.4^{+9.3}_{-8.8}$
SN 2021inl	Present	$0.0100^{+0.0021}_{-0.0026}$	81^{+13}_{-12}
SN 2021sjt	Present	$0.49^{+0.18}_{-0.13}$	19^{+13}_{-13}
SN 2021acnz	Present	$0.232^{+0.080}_{-0.054}$	$322.7^{+3.0}_{-2.1}$
SN 2022nwx	Present	$0.0250^{+0.0091}_{-0.0078}$	94^{+15}_{-15}
SN 2022oqm	Present	$0.0495^{+0.0054}_{-0.0051}$	1319^{+356}_{-346}
SN 2023er	Present	$0.043^{+0.018}_{-0.010}$	$57.3^{+3.0}_{-2.8}$
AT 2021zfp	Possible	≤ 0.62	≤ 80
AT 2024aaab	Possible	≤ 0.013	≤ 24
SN 2018ckd	Possible	≤ 0.62	≤ 56
SN 2018dbg	Possible	≤ 0.36	≤ 24
SN 2018kqr	Possible	≤ 0.013	≤ 220
SN 2019gau	Possible	≤ 0.62	≤ 130
SN 2019ofm	Possible	≤ 0.65	≤ 110
SN 2019ouq	Possible	≤ 0.61	≤ 310
SN 2023er	Possible	≤ 0.46	≤ 24
SN 2024jgw	Possible	≤ 0.53	≤ 56
SN 2024uai	Possible	≤ 0.62	≤ 140

Notes. Derived envelope mass and radius values for all 'present bump' and 'possible bump' objects of the 26 objects with photometric observations pre-peak from our total sample.

Table B.6. Velocities and associated errors of the [Ca II] and [O I] $\lambda\lambda$6300,6364 emission features.

Object	$v_{\mathrm{Ca\,II}}$ [km s^{-1}]	$v_{\mathrm{O\,I}}$ [km s^{-1}]	Phase [days]
SN 2000ds	−245.40 ± 86.55	−161.12 ± 192.44	14.0
SN 2001co	−303.30 ± 157.22	-	93.0
SN 2001co	−302.86 ± 131.73	-	104.0
SN 2001co	−514.11 ± 208.70	-	125.0
SN 2003H	218.65 ± 146.06	527.58 ± 200.18	75.0
SN 2003H	−119.77 ± 99.26	527.58 ± 200.18	99.0
SN 2003dg	−1107.79 ± 137.60	−1456.31 ± 220.53	70.0
SN 2003dr	444.54 ± 93.57	529.21 ± 195.95	40.0
SN 2005E	−2139.47 ± 104.23	180.38 ± 197.95	-3.7
...	...	...	...

Notes. Each emission line velocity is presented only for S/N >3. The full table can be found at the CDS.

Table B.7. Sub-classifications of confirmed Ca-strong objects.

Object	$a_{\mathrm{Si\,II}\,\lambda\lambda6150} \pm \sigma_{a_{\mathrm{Si\,II}\,\lambda\lambda6150}}$	Sub-category
SN 2005E	0.093 ± 0.023	Ca-strong Ib/c
SN 2010et	0.297 ± 0.023	Ca-strong Ib/c
iPTF11kmb	0.078 ± 0.010	Ca-strong Ib/c
iPTF15eqv	0.111 ± 0.009	Ca-strong Ib/c
SN 2016hgs	0.215 ± 0.036	Ca-strong Ib/c
SN 2016hnk	0.639 ± 0.014	Ca-strong Ia
SN 2018gwo	0.253 ± 0.037	Ca-strong Ib/c
SN 2018kjy	0.137 ± 0.018	Ca-strong Ib/c
SN 2019ehk	0.044 ± 0.027	Ca-strong Ib/c
SN 2019gau	0.145 ± 0.006	Ca-strong Ib/c
SN 2019kqr	0.219 ± 0.007	Ca-strong Ib/c
SN 2019ouq	0.063 ± 0.026	Ca-strong Ib/c
SN 2019pof	0.181 ± 0.002	Ca-strong Ib/c
AT 2021acnz	0.073 ± 0.002	Ca-strong Ib/c
SN 2021gno	0.289 ± 0.026	Ca-strong Ib/c
SN 2021sjt	0.208 ± 0.005	Ca-strong Ib/c
AT 2022nwx	0.200 ± 0.001	Ca-strong Ib/c
SN 2022oqm	0.202 ± 0.002	Ca-strong Ib/c
SN 2023er	0.108 ± 0.029	Ca-strong Ib/c
SN 2023xwi	0.165 ± 0.036	Ca-strong Ib/c
AT 2024aaab	0.214 ± 0.007	Ca-strong Ib/c
SN 2024jgw	0.091 ± 0.011	Ca-strong Ib/c
SN 2024uai	0.121 ± 0.033	Ca-strong Ib/c
iPTF09dav	0.458 ± 0.105	Ambiguous
SN 2018lqo	0.350 ± 0.022	Ambiguous
SN 2018lqu	0.256 ± 0.072	Ambiguous
SN 2019ofm	0.361 ± 0.008	Ambiguous
SN 2021inl	0.177 ± 0.157	Ambiguous

Notes. The sub-classifications are defined by the line depth of the Si II λ6150 absorption feature – $a_{\mathrm{Si\,II}\,\lambda6150}$ – outlined in Sun & Gal-Yam (2017) and De et al. (2020). The following SNe do not have a spectrum in the correct phase range to obtain a measurement: SN 2000ds, SN 2001co, SN 2003dg, SN 2003dr, SN 2003H, SN 2005cz, SN 2007ke, iPTF12bho, SN 2018ckd, SN 2018dbg, SN 2019hty, SN 2019pxu, SN 2019txr, AT 2021zfp, SN 2021inl, SN 2023fhk, SN 2023ugn, and SN 2024uj.